CELL BIOLOGY

Temporal control of the integrated stress response by a stochastic molecular switch

Philipp Klein[1]†, Stefan M. Kallenberger[2,3,4]†, Hanna Roth[1], Karsten Roth[1]‡, Thi Bach Nga Ly-Hartig[5,6], Vera Magg[1], Janez Aleš[7]§, Soheil Rastgou Talemi[8], Yu Qiang[9], Steffen Wolf[7]||, Olga Oleksiuk[1]¶, Roma Kurilov[2]#, Barbara Di Ventura[2], Ralf Bartenschlager[1,10], Roland Eils[2,3], Karl Rohr[9], Fred A. Hamprecht[7], Thomas Höfer[8], Oliver T. Fackler[11], Georg Stoecklin[5,6], Alessia Ruggieri[1]***

Stress granules (SGs) are formed in the cytosol as an acute response to environmental cues and activation of the integrated stress response (ISR), a central signaling pathway controlling protein synthesis. Using chronic virus infection as stress model, we previously uncovered a unique temporal control of the ISR resulting in recurrent phases of SG assembly and disassembly. Here, we elucidate the molecular network generating this fluctuating stress response by integrating quantitative experiments with mathematical modeling and find that the ISR operates as a stochastic switch. Key elements controlling this switch are the cooperative activation of the stress-sensing kinase PKR, the ultrasensitive response of SG formation to the phosphorylation of the translation initiation factor eIF2α, and negative feedback via GADD34, a stress-induced subunit of protein phosphatase 1. We identify GADD34 messenger RNA levels as the molecular memory of the ISR that plays a central role in cell adaptation to acute and chronic stress.

INTRODUCTION

Mammalian cells maintain cellular homeostasis and promote survival by integrating a multitude of extrinsic and intrinsic signals into a spatially and temporally regulated response. Adverse conditions, such as oxidative stress, endoplasmic reticulum (ER) stress, and virus infections, are detected by four specialized cytosolic sentinels that belong to the eukaryotic translation initiation factor 2-alpha (eIF2α) kinase family of serine/threonine kinases. They initiate the integrated stress response (ISR) by immediately phosphorylating eIF2α (*1*), interfering with formation of the eIF2–guanosine triphosphate–tRNAi^{Met} ternary complex and thus inhibiting translation initiation (*2*). As a consequence, polysomes disassemble and nontranslating messenger RNAs (mRNAs) phase separate together with RNA binding proteins into membraneless biomolecular condensates called stress granules (SGs) (*3*). Among the eIF2α kinases, protein kinase R (PKR) is an interferon (IFN)–induced kinase (*4*) that mediates translation suppression in response to replication of many RNA viruses. PKR activation was initially described to result from binding to double-stranded (ds) RNA of diverse viral origin such as viral replication intermediates or transcripts containing stem loop structures generated during infection. However, other sources of cellular dsRNAs, including mitochondrial dsRNA, circular RNAs, and small nucleolar RNAs, also control its activation (*5*). PKR dimerization, which is required for its activation, leads to autophosphorylation of the PKR kinase domain, most notably at threonine-446, and to structural rearrangements that facilitate binding to eIF2α (*6*–*9*).

Translation shutdown feeds back into the regulation of eIF2α phosphorylation by up-regulating growth arrest and DNA damage–inducible 34 (GADD34), a stress-induced regulatory subunit of protein phosphatase 1 (PP1) (*10*) that acts as an antagonist of the eIF2α kinases and mediates eIF2α dephosphorylation. This system allows the cell to integrate different cues and adjust the degree of translational suppression during the course of stress responses. We previously found an extreme case of such temporal control, whereby hepatitis C virus (HCV), a major human pathogen causing chronic liver infection, induces a sustained cellular stress response characterized by recurrent alternating translational Off and On states that are, respectively, accompanied by the assembly and disassembly of SGs. Notably, the duration of Off and On states was highly variable in individual cells and not synchronous between cells. At the molecular level, the fluctuating SG response was dependent on PKR and GADD34 and strongly enhanced by treatment of HCV-infected cells with IFN-α (*11*). However, the molecular mechanisms underlying the apparently oscillatory nature of this response have not been elucidated.

Oscillations are observed in numerous biological systems, including the circadian clock, metabolism, signaling, cell division, and

[1]Department of Infectious Diseases, Molecular Virology, Center for Integrative Infectious Diseases Research, Heidelberg University, Heidelberg, Germany. [2]Division of Theoretical Bioinformatics, German Cancer Research Center (DKFZ), Heidelberg, Germany. [3]Digital Health Center, Berlin Institute of Health (BIH) and Charité, Berlin, Germany. [4]Medical Oncology, National Center for Tumor Diseases, Heidelberg University, Heidelberg, Germany. [5]Division of Biochemistry, Mannheim Institute for Innate Immunoscience (MI3), Medical Faculty Mannheim, Heidelberg University, Mannheim, Germany. [6]Center for Molecular Biology of Heidelberg University (ZMBH), DKFZ-ZMBH Alliance, Heidelberg, Germany. [7]HCI/IWR, Heidelberg University, Heidelberg, Germany. [8]Division of Theoretical Systems Biology, German Cancer Research Center (DKFZ), Heidelberg, Germany. [9]Biomedical Computer Vision Group, BioQuant, IPMB, Heidelberg University, Heidelberg, Germany. [10]Division Virus-Associated Carcinogenesis, German Cancer Research Center (DKFZ), Heidelberg, Germany. [11]Department of Infectious Diseases, Integrative Virology, Center for Integrative Infectious Diseases Research, Heidelberg University, Heidelberg, Germany.
*Corresponding author. Email: alessia.ruggieri@med.uni-heidelberg.de
†These authors contributed equally to this work.
‡Present address: Cluster of Excellence Machine Learning for Science, University of Tübingen, Tübingen, Germany.
§Present address: BASF SE, GDB/EB, Ludwigshafen am Rhein, Germany.
||Present address: MRC Laboratory of Molecular Biology, Cambridge, UK.
¶Present address: Joint HIH-CIN Imaging Cluster, Centre for Integrative Neuroscience (CIN), Tübingen, Germany.
#Present address: Applied Bioinformatics Division, German Cancer Research Center (DKFZ), Heidelberg, Germany.
**Present address: Faculty of Biology, Institute of Biology II, University of Freiburg, Freiburg, Germany; Centers for Biological Signalling Studies BIOSS and CIBSS, University of Freiburg, Freiburg, Germany.

development (*12*, *13*). Oscillating systems are characterized by signal amplitude and periodicity covering a large range of time scales from seconds, in the case of calcium signaling, to hours, e.g., for bursts of tumor suppressor p53 expression upon DNA damage or for the circadian clock (*14*). However, not every dynamic biochemical system characterized by recurring bursts in signals necessarily constitutes an oscillator. Biochemical processes are subjected to biological noise that affects the kinetics of cellular reactions, particularly involving factors of low abundance, and influences the behavior of the response, thus generating cell-to-cell variability (*15*–*18*).

Here, we set out to model the recurrent alternating stress response, using HCV infection as a model for chronic stress response, with the aim to understand the molecular mechanisms that govern its establishment and maintenance over long periods of time. To this end, we developed a quantitative deterministic mathematical model that describes the components and reactions involved in the ISR to oxidative stress, ER stress, and, more specifically, the dsRNA-induced SG response. To approximate our cell system as closely as possible, we experimentally determined a large set of key species concentration ranges using bulk and single-cell methods. While our observations first suggested that the ISR signaling network shares common features of an oscillator, we found that HCV-induced SG fluctuations result from repetitive stochastic transitions between On and Off states that are regulated by cell-to-cell variability in PKR and dsRNA concentrations. Our results identified GADD34 mRNA levels as the molecular memory of the ISR, which plays a crucial role in adaptation to acute and chronic stress.

RESULTS

The fluctuating SG response to HCV infection exhibits a stochastic switch behavior with memory

To accurately characterize the dynamics of the cellular stress response to HCV infection, we monitored SG formation using long-term live-cell microscopy with high time resolution. Human hepatocarcinoma-derived Huh7 cells stably expressing the SG protein T cell–restricted intracellular antigen-1 (TIA-1) fused to the yellow fluorescent protein (YFP) were infected with HCV-like particles [HCV trans-complemented particles (HCV_{TCP})], which encode the fluorescent protein mCherry fused to the viral nonstructural protein NS5A and *Renilla* luciferase for the measurement of viral replication (fig. S1A). As replication reached its maximum, i.e., 48 hours after infection (fig. S1B), SG response dynamics was monitored for 72 hours in infected cells that were either left untreated or treated with IFN-α (fig. S1C). Images were acquired with 15-min intervals to ensure the detection of short SG phases while limiting phototoxicity (Fig. 1A and movies S1 and S2). Automated single-cell tracking in such long-term time lapses is challenging because of the relatively long interval between acquisition frames, cell division events, and the increasing cell density toward the end of the acquisition period (*19*). We therefore developed a semiautomated image processing pipeline primarily based on the machine-learning toolkit ilastik (*20*) and analyzed the appearance and disappearance of SGs (here defined as SG-On and SG-Off phases, respectively) in single cells over time (Fig. 1, B and C, and fig. S1D). As previously observed (*11*), SGs were extremely rare in uninfected cells (fig. S2A). In HCV-infected cells that were not exposed to IFN-α, most cells displayed 0.5 to 1.5 SG-On phases per day (Fig. 1D, left graph, and fig. S2A). This number increased upon addition of IFN-α, with most cells having 1 to 2.5 SG-On phases per day (Fig. 1D, right graph). SG phases did not exhaust over time (Fig. 1C). The comparative analysis of SG properties and infection level—as measured by mCherry-NS5A fluorescence intensity—revealed a slight positive correlation between the infection level and the total number of SGs as well as the number of SG phases, and a negative correlation with the SG integral (total duration of SG presence) and duration (mean phase duration) (fig. S2B), suggesting a possible role of SGs in host defense as reported for other viral infections (*5*).

SG fluctuations could result from an oscillator mechanism, which has a fixed period possibly disturbed by noise effects, or from the random switching between SG-On and SG-Off states, a so-called random telegraph process, which has no fixed period because the moments in which cells switch from one state to the other are not influenced by the time already elapsed. To get more insight into the quality of the SG fluctuations, we simulated these models computationally and compared the results to experimental single-cell SG response time series (Fig. 1E and section S1). We analyzed the degree of SG phase periodicity from each time series using the frequency spectrum (obtained via the Fourier transform) and the autocovariance function. In contrast to a simulated oscillator distinguished by distinct peaks in the frequency spectrum and an autocovariance function alternating between positive and negative values (Fig. 1E, top), SG response time series revealed the absence of a defined frequency, both in the presence and in the absence of IFN-α (Fig. 1F). The autocovariance function showed a continuous decline similar to that of the telegraph process (Fig. 1E, middle). However, unlike the telegraph process, it even reached slightly negative values, particularly for untreated cells (Fig. 1G), suggesting a negative correlation between SG-On and SG-Off phase length. The analysis of the experimental SG phase length distribution in HCV-infected cells indicated preferred phase lengths and validated this correlation. Observations were well described by two joint gamma distributions (fig. S2C). Simulations of such a gamma-distributed two-state process (Fig. 1E, bottom) reliably recapitulated the frequency spectra and autocovariance functions of the experimental observations (Fig. 1, F and G). In addition, calculated autocovariance exponential decay times were reduced upon IFN-α treatment (from 4 to 2 hours; fig. S2D), reflecting the occurrence of shorter SG-On and SG-Off phases under this condition. Together, our results suggest that SG fluctuations are described neither by an oscillator nor by a simple telegraph process but rather by a stochastic switching process with memory. Specifically, the moment at which cells switch SG phase is negatively correlated with the duration of the preceding SG phase.

Network topology of the eIF2α-mediated signaling pathway

We previously uncovered that SG fluctuations during chronic HCV infection result from antagonistic activities of PKR and GADD34-PP1 on eIF2α phosphorylation (*11*). To understand how these main regulators shape this peculiar SG response dynamics in single cells, we developed a deterministic mathematical model based on ordinary differential equations (ODEs) that describes the eIF2α-dependent signaling pathway in response to stress, particularly to dsRNA, assuming a homogeneous and synchronized cell population. The model was structured into three independent but connected modules (Fig. 2A). The upper stress-sensing module describes the activation of the stress kinases, specifically PKR by dsRNA, but also heme-regulated inhibitor (HRI) and PKR-like (ER) kinase (PERK) by

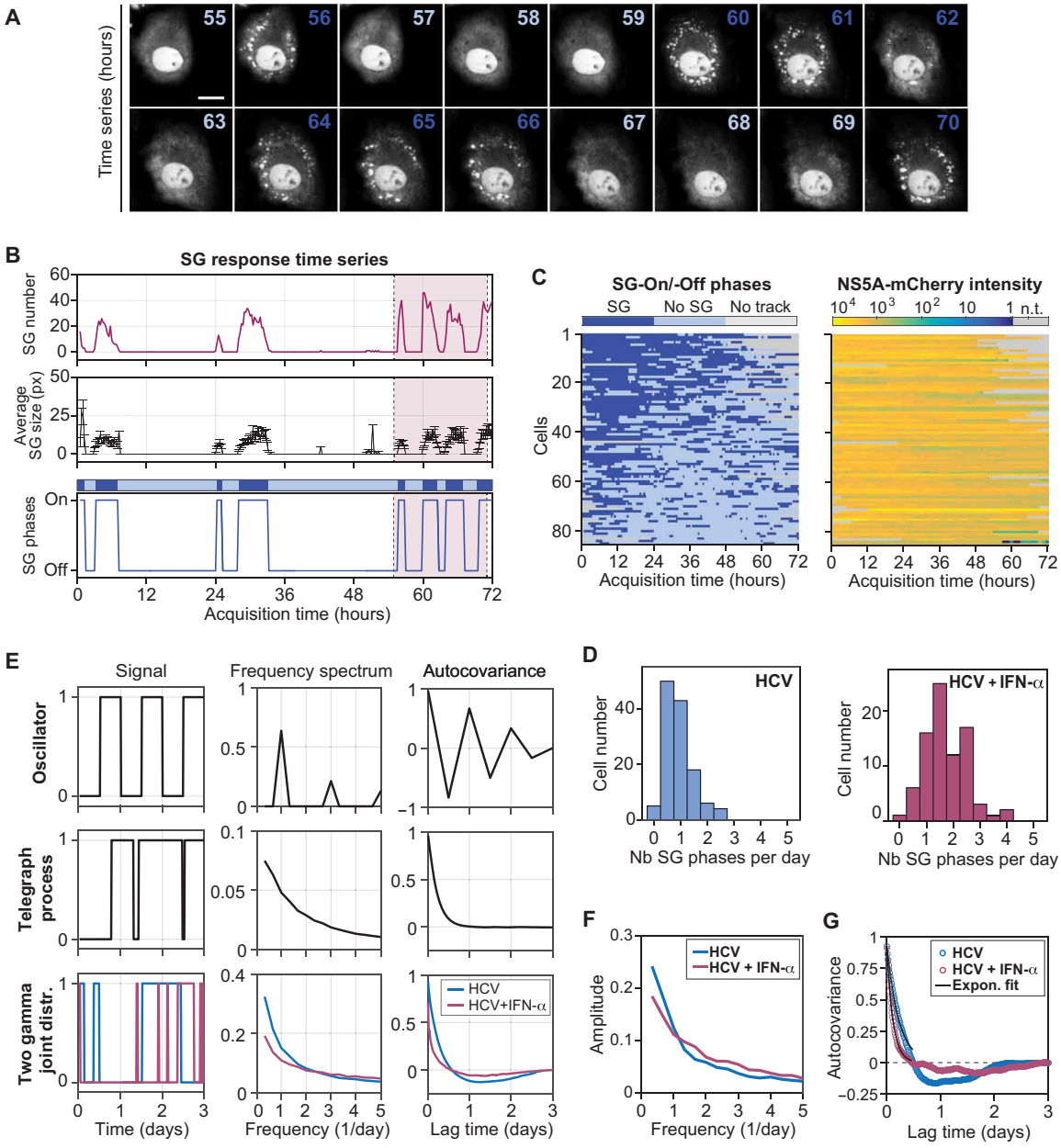

Fig. 1. Time-resolved analysis of HCV-induced SG phases. (**A**) Still images of a cropped section of the 72-hour time-lapse movie of HCV-infected Huh7 YFP-TIA1 cells treated with IFN-α (YFP-channel). A representative cell is shown with 1-hour interval for the time period 55 to 70 hours. Dark blue time label: SG-On phases; light blue time label: SG-Off phases. Scale bar, 25 μm. (**B**) Example of time-lapse analysis output for the cell shown in (A). The number of SGs (top) and the average SG size in pixel (middle) were analyzed for each frame and allowed defining SG-On and SG-Off phases (bottom). The pink-shaded area corresponds to the time period 55 to 70 hours shown in (A). A schematic of the SG response time series is shown at the top; dark blue regions: SG-On phases; light blue regions: SG-Off phases. (**C**) Analysis of multiple single-cell SG response time series ($n = 85$). Left: SG-On and SG-Off phases. Right: Infection levels as measured by NS5A-mCherry signal intensity for the corresponding cells. n.t., no track. (**D**) Number of SG phases per day in the absence (left) or presence of IFN-α (right). (**E**) Simulations of oscillator, random telegraph process, or joint gamma distributions ($n = 500$). Left: Type of signal response. Middle: Frequency spectrum. Right: Autocovariance function. (**F**) Average frequency spectra (Fourier transforms) of experimental single-cell SG response time series. (**G**) Autocorrelation functions of experimental single-cell SG response time series.

different mechanisms [e.g., treatment with sodium arsenite and thapsigargin, respectively (*21*)], which all resulted in different dynamics of eIF2α phosphorylation. The decision module shared between the three stress kinases is composed of eIF2α, whose phosphorylation leads to translation repression and SG formation. The shared downstream recovery module describes the transcriptional and translational activation of GADD34, which represents a negative feedback loop that promotes return to homeostasis through eIF2α dephosphorylation, SG disassembly, and translation reinitiation.

To constrain the mathematical model for making quantitative predictions, we first measured the mean abundance per cell of the key proteins, i.e., PKR, eIF2α, and GADD34. Protein amounts were

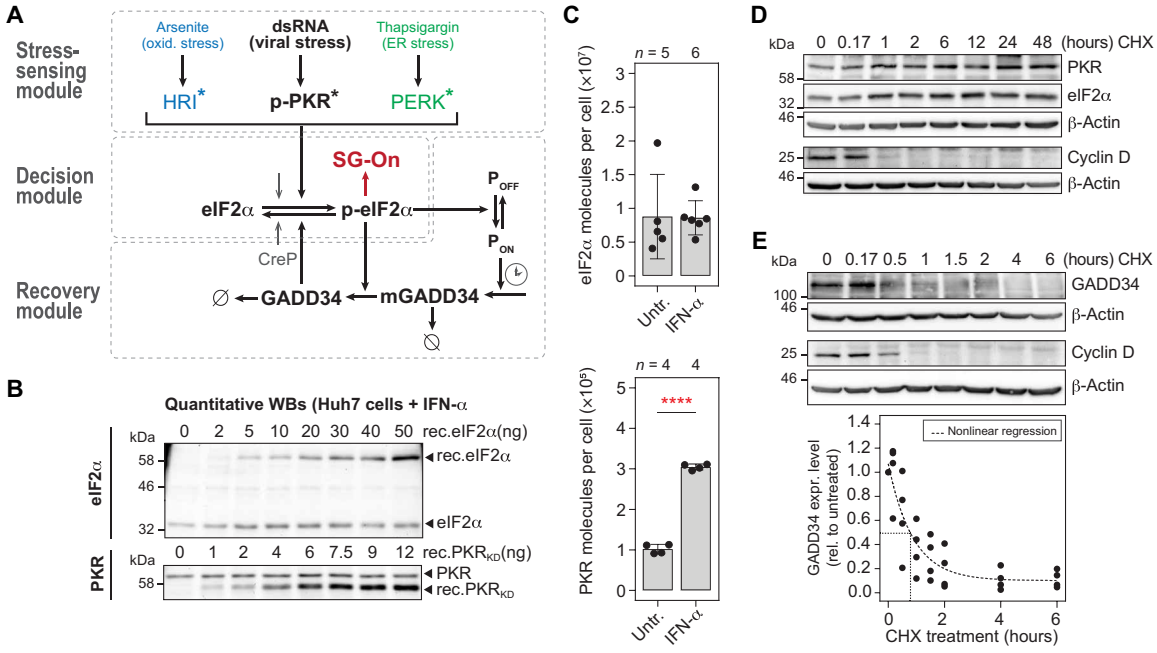

Fig. 2. Deterministic mathematical model of the cellular ISR. (**A**) Schematic representation of the parameters and reactions included in the mathematical model. The stress-sensing module represents the activation of stress kinases. PKR is activated by binding to dsRNA (viral stress, p-PKR*), HRI by arsenite treatment (oxidative stress, HRI*), and PERK by thapsigargin (ER stress, PERK*). Active stress kinases signal to the decision module, where upon crossing a p-eIF2α level threshold will trigger SG formation (SG-On). Elevated p-eIF2α levels activate the recovery module consisting of the GADD34 negative feedback loop, i.e., *ppp15R1a* promoter activation (P_{OFF} to P_{ON}) with time delay (clock symbol), GADD34 transcription (mGADD34), and protein synthesis (GADD34). In turn, GADD34 dephosphorylates eIF2α and thereby resumes translation. Gray arrow, basal eIF2α dephosphorylation by CReP, the constitutive regulatory subunit of PP1. Ø, degradation. (**B** and **C**) Absolute quantification of eIF2α and PKR mean molecule numbers in Huh7 YFP-TIA1 cells, in the absence and presence of IFN-α. (B) Representative quantitative Western blot analysis of eIF2α and PKR. (C) Estimated eIF2α and PKR mean molecule number per cell (±SD). Number of repeats (*n*) and statistical significance compared to untreated cells (untr.) are indicated; ****$P < 0.0001$. (**D** and **E**) Determination of protein half-lives by CHX pulse experiments and Western blot analyses. (D) PKR and eIF2α half-lives ($n = 3$). (E) GADD34 ($n = 4$). Black line, best nonlinear fit.

measured by quantitative Western blot analysis using standard dilutions of recombinant glutathione *S*-transferase (GST)–tagged eIF2α and PKR as reference (Fig. 2B and fig. S3A). As expected for a constitutively expressed protein, the levels of eIF2α did not vary upon addition of IFN-α. However, the levels of PKR increased threefold (Fig. 2C). By measuring the mean volume of Huh7 cells (fig. S3B), we deduced the corresponding mean concentrations of approximately 2.24 mM for eIF2α, 25.24 nM for PKR in untreated cells, and 75.48 nM for PKR in IFN-α–treated cells. As no basal expression of GADD34 was detected in unstressed cells, we measured the amount of GADD34 that could be induced upon treatment with thapsigargin, a chemical inducer of ER stress. Since endogenous, overexpressed, and even recombinant GADD34 are extremely sensitive to degradation (fig. S3C), we used an indirect approach and first quantified GADD34 levels in Huh7 cells stably expressing GADD34–enhanced green fluorescent protein (eGFP) using a titration of recombinant eGFP. These calibrated lysates served as reference for GADD34 measurements in Huh7 cells treated with thapsigargin. Thereby, we estimated that the mean concentration of stress-induced GADD34 typically reaches 8×10^3 molecules per cell (equivalent to 2 nM) (fig. S3D).

Last, degradation rates of species involved in feedback loops are linked to time delays and thereby facilitate oscillations (*22*). We hence determined protein turnover by cycloheximide (CHX) chase experiments using the short-lived protein cyclin D as a control. PKR and eIF2α were found to be long-lived proteins (Fig. 2D and fig. S3E), whose degradation rates are therefore negligible for the model. In turn, stably overexpressed GADD34 was labile (Fig. 2E) in agreement with previous reports (*23*). Comparison of two possible degradation models, Michaelis-Menten kinetics and exponential decay, indicated that GADD34 degradation is described more accurately by exponential decay—implying that GADD34 degradation was not saturated—with an estimated half-life of approximately 37 min (section S3).

Together, this first set of quantitative measurements yielded mean concentrations of the main model species that will serve as boundary conditions of the deterministic mathematical model. In addition, we found PKR and eIF2α turnover to be negligible parameters for the model, whereas GADD34 is short-lived, a feature that might facilitate the generation of oscillations.

Dose-response analyses reveal the switch-like behavior of SG formation

Following the quantification of these key parameters, we sought to characterize the central decision module of the model and determined the level of phosphorylated eIF2α (p-eIF2α) at which cells transition from an SG-Off to an SG-On phase. To this end, we performed dose-response analyses and measured the percentage of SG-positive cells at the population level as a function of dsRNA concentration. Since the precise nature and length of dsRNA intermediates produced

during HCV infection are unknown, we synthesized in vitro dsRNAs of variable lengths [100, 200, and 400 base pairs (bp); fig. S4A] and compared their potential to activate PKR upon transfection into cells (fig. S4B). PKR activity was assessed by measuring (i) eIF2α and PKR phosphorylation levels using Western blot analysis (Fig. 3, A and B, and fig. S4C), (ii) the percentage of p-eIF2α relative to total eIF2α using Phos-tag gel analysis (Fig. 3, A and B), and (iii) the percentage of SG-positive cells by immunofluorescence analysis (Fig. 3C). Of note, although 400-bp dsRNA triggered the highest levels of PKR activation, it formed additional secondary structures under nonreducing conditions (fig. S4A). We thus chose 200-bp dsRNA for the following dose-response experiments. At best, dsRNA transfection induced 25% eIF2α phosphorylation (Fig. 3B) and 40% SG-positive cells (Fig. 3C). PKR activation followed a bell-shaped curve as reflected by a significant decrease in the levels of phosphorylated PKR (p-PKR), p-eIF2α, and in the number of SG-positive cells, at higher dsRNA concentrations. This is consistent with earlier reports (*24*) and suggests inhibition of PKR at high levels of dsRNA.

These results combined with the possibility that the transfection approach does not homogeneously deliver dsRNA to all cells represented a significant technical limitation to determine the half-maximal dose of p-eIF2α causing SG formation. Therefore, we turned to chemical stress inducers and determined p-eIF2α thresholds upon treatment with sodium arsenite (Fig. 3, D and E, and fig. S4D) and thapsigargin (fig. S4, E to J), which trigger HRI-dependent oxidative stress and PERK-dependent ER stress, respectively (*21*), and synchronously induced SG formation in all cells at higher concentrations (Fig. 3F and fig. S4H). When the percentage of SG-positive cells was plotted against the percentage of p-eIF2α (Fig. 3G), we observed an ultrasensitive sigmoidal SG response curve with a steep transition over a narrow range of chemical stress inducer concentrations. The half-maximal SG response occurred when approximately 38.5 and 30.6% eIF2α was phosphorylated upon arsenite and thapsigargin treatment, respectively, defining the level at which cells switched from an SG-Off to an SG-On phase. The steepness of the sigmoidal curve estimated by the Hill function revealed notably high coefficients of 14.8 and 18 for arsenite and thapsigargin treatment, respectively, indicating a high degree of cooperativity.

Together, the characterization of the core decision module identified a threshold level of p-eIF2α at which cells transition from an SG-Off to an SG-On phase. The steep SG response curve revealed the "switch-like" behavior of SG formation when cells were exposed to different chemical stress inducers, with different thresholds for each of the eIF2α kinases. Of these, PKR emerged as the only eIF2α kinase whose activation is dampened at higher dsRNA concentrations.

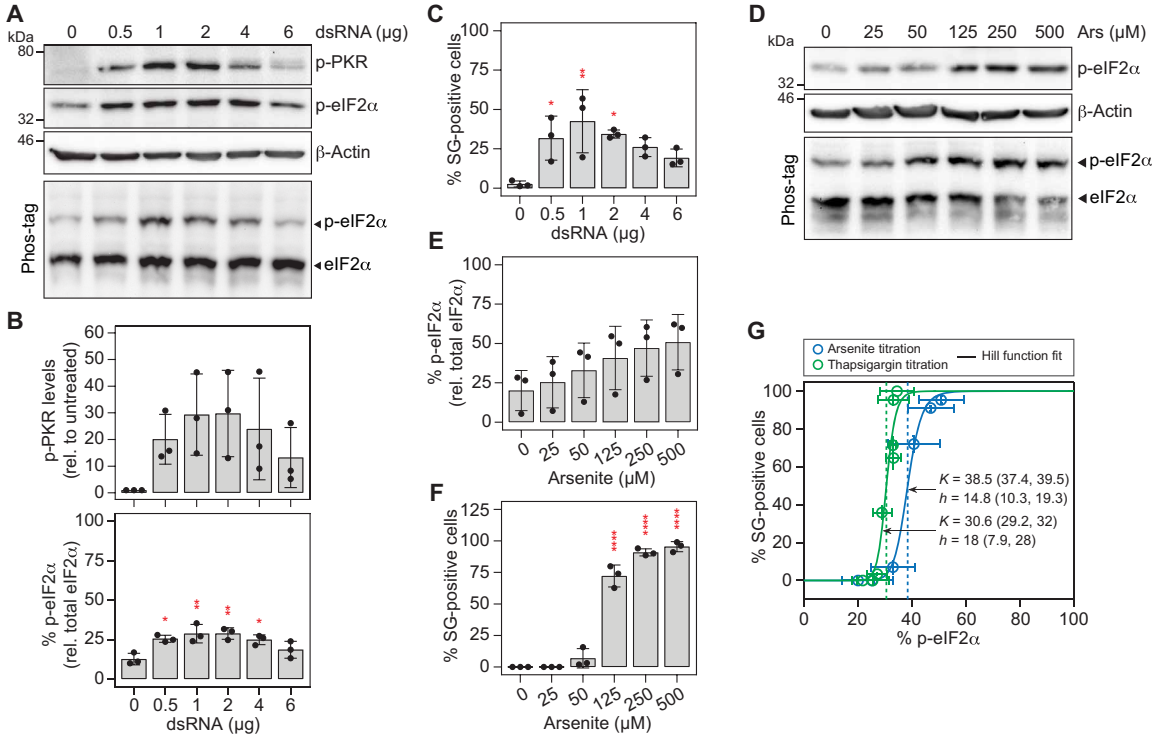

Fig. 3. SG formation is a switch-like process. (**A** to **C**) Activation of PKR in Huh7 YFP-TIA1 cells transfected with increasing amounts of 200-bp dsRNA ($n = 3$). (A) Representative Western blot analysis of p-PKR and p-eIF2α expression levels. Expression levels of β-actin served as loading control. The percentage of p-eIF2α was analyzed by Phos-tag polyacrylamide gel. (B) Shown are quantifications of mean p-PKR expression levels (±SD) normalized to the loading control and relative to untreated cells (top) and quantifications of the mean p-eIF2α percentage (±SD). Statistical significance is indicated compared to untreated cells. (C) The presence of SGs in transfected cells was analyzed by fluorescence microscopy (for each condition, $n > 100$). Shown are mean percentages ± SD. Statistical significance is indicated compared to untreated cells. $^{*}P < 0.05$, $^{**}P < 0.01$. (**D** to **F**) Induction of oxidative stress in Huh7 YFP-TIA1 cells by treatment with increasing concentrations of arsenite for 45 min ($n = 3$). (D) Representative Western blot and Phos-tag analyses. Shown are mean percentages ± SD of p-eIF2α (E) and SG-positive cells (for each condition, $n > 100$) (F). Statistical significance is indicated compared to untreated cells; $^{****}P < 0.0001$. (**G**) Dose-response analysis and determination of the p-eIF2α level that results in formation of SGs in 50% of cells upon treatment with arsenite [related to (F); $n = 3$] and thapsigargin (related to fig. S4, E to H; $n = 3$).

PKR activation results from its cooperative recruitment to dsRNA

We next focused on characterizing the parameters and reactions involved in the stress-sensing module upstream of eIF2α. To understand PKR activation in more detail, we established an in vitro kinase assay using recombinant full-length His-tagged PKR and His-tagged eIF2α and quantitatively assessed the impact of increasing dsRNA length and molarity on PKR activation. Addition of both 100- and 200-bp dsRNAs led to a bell-shaped activation of PKR, which reached its maximum at 10 nM dsRNA, irrespective of the dsRNA length (Fig. 4A and fig. S5A). Under these experimental conditions, i.e., in the absence of phosphatase, full eIF2α phosphorylation was reached at slightly lower dsRNA concentrations (fig. S5B). In contrast to 100- and 200-bp dsRNAs, 40-bp dsRNA was much less potent in activating PKR, leading to a maximum of only 25% of eIF2α being phosphorylated (fig. S5, B and C).

Since the individual steps of PKR activation are not fully understood, we developed mathematical models consisting of coupled ODEs and tested which model variant could optimally explain our experimental dataset (section S2 and table S1). Starting with a simple model describing PKR dimerization upon binding to dsRNA (figs. S6A and S7, variant 1), several models with stepwise increasing complexity were developed and calibrated with the experimental datasets obtained in cell transfection and in vitro kinase assays (figs. S6A and S7 and table S1). We sequentially tested whether the following aspects had to be included in the model (Fig. 4B): (i) dependency of the PKR affinity to dsRNA on fragment length, (ii) dependency of the number of PKR binding sites on fragment length, (iii) formation of PKR oligomers ($n = 2…6$), (iv) cooperative binding of PKR to dsRNA resembling formation of high oligomers of active PKR, and (v) *cis* (intramolecular) and *trans* (intermolecular) phosphorylation of/between active PKR molecules. Models were fitted at steady state, assuming that binding and phosphorylation reactions were fast. The corrected Akaike information criterion was used for model selection (section S2 and fig. S6, B and C). Testing the contribution of previously described PKR *cis* or *trans* interactions (*7*, *25*, *26*) did not substantially improve model fits (Fig. 4C and fig. S7, variants 4 to 5.1). In the optimal model variant, cooperative PKR recruitment to dsRNA was described by sigmoidal kinetics reflected by a Hill equation, whereas other reactions were described by mass-action kinetics. Together, the model that most closely recapitulated the experimental results (Fig. 4, D and E, and fig. S7, variant 3) revealed three important features of PKR activation: (i) different affinities for PKR to dsRNA of varying lengths, (ii) dependency of PKR-binding site numbers on dsRNA fragment lengths, and (iii) the cooperative recruitment to dsRNA and oligomerization of PKR, which would be consistent with higher-order oligomerization of active PKR.

Quantitative characterization of the GADD34 negative feedback loop

We next explored the parameters involved in the recovery module (Fig. 2A) consisting of the GADD34 negative feedback loop (*27*). Stress and phosphorylation of eIF2α trigger the translation of the activating transcription factor 4 (ATF4) (*28*). In turn, ATF4 activates the CCAAT/enhancer binding protein homologous protein (CHOP) and, ultimately, in complex with CHOP, the promoter of the *ppp1r15a* gene encoding GADD34 (*28*, *29*). However, in IFN-competent cells, GADD34 transcription is additionally regulated by the IFN regulatory factor (IRF) 3 and IRF7, downstream of the RNA sensing innate immune pathway (*30*, *31*). We used fluorescence in situ hybridization (FISH) to investigate GADD34 transcriptional regulation in HCV-infected Huh7 cells in the absence and presence of IFN-α treatment (Fig. 5A). This single-cell approach accounted for the low number of infected cells and avoided underestimation in case of bulk measurement. In addition, cells were costained with specific fluorescent probes hybridizing to HCV positive-sense single-stranded [(+)ss] RNA genome and polyadenylated (polyA) mRNA, whereby GADD34 mRNA and HCV infection levels could be directly correlated in SG-negative and SG-positive cells (Fig. 5A and fig. S8, A and B). Fluorescent probes directed against *Bacillus subtilis* dihydrodipicolinate reductase (dapB), a noneukaryotic transcript, served as control for unspecific binding (neg. ctrl). To assess the contribution of the IRF3/IRF7 pathway in GADD34 transcriptional activation, we circumvented activation of the p-eIF2α-ATF4-CHOP pathway by using Huh7 PKR knockout (PKR_{KO}) cells. As expected, the absence of PKR abolished SG formation in response to HCV infection. Since neither infection nor treatment with IFN-α elicited GADD34 transcription in PKR_{KO} cells (fig. S8, C and D), we concluded that IRF3/IRF7-dependent GADD34 activation is negligible in Huh7 cells. This allowed us to develop a mathematical model that specifically describes the stress-induced GADD34 negative feedback loop without taking into account innate immune signaling (Fig. 2A). In naïve Huh7 cells, stress induced by HCV infection in the presence of IFN-α resulted in a 2.5-fold increase in the mean number of GADD34 transcripts in SG-positive cells. However, the cell-to-cell variability was more substantial, almost 20-fold (Fig. 5A). Of note, this cell-to-cell variability was notably smaller for transcriptional induction of PKR by IFN-α (fig. S9, A and B). In addition, GADD34 transcript levels only weakly correlated with the number of HCV genome copies per cell (fig. S9C). This quantitative information was then used to assess the SG response at the population level in a dose-response manner based on GADD34 mRNA levels (section S4.7 and fig. S10A).

Time delay is an important parameter of negative feedback loops that exist in numerous mammalian signaling pathways in response to external stimuli (*32*) and may result in network oscillations (*33*). For GADD34, this time delay (depicted as a clock in Fig. 2A) includes the time required for *ppp1r15a* promoter activation and upstream open reading frame (uORF)–mediated translation of GADD34 (*34*). We therefore analyzed p-eIF2α and GADD34 induction kinetics in cells treated with 2 μM thapsigargin, a dose at which all cells formed SGs. Levels of p-eIF2α rapidly increased, reached a maximum after 1 hour, and returned to basal levels about 4 hours after treatment. GADD34 started to visibly increase at 1.5 hours after treatment and reached a maximum at 5 hours (fig. S11, A and B).

Last, we sought to determine the levels at which GADD34 antagonizes the activity of eIF2α kinases, thereby allowing cells to resume translation and switch from an SG-On to an SG-Off phase. To this end, we ectopically expressed increasing levels of GADD34 using lentiviral transduction and challenged cells with thapsigargin for 1 hour. At this time point, endogenous GADD34 was not yet detectable (see fig. S11, A and B), and all cells transduced with a control lentivirus formed SGs (fig. S11C). GADD34 expression reduced the level of p-eIF2α and SG formation already at the lowest concentration. We found about 11.6 nM GADD34 protein per cell to antagonize SG formation in 50% of the cells, and about fourfold more was required to antagonize SG formation in all cells (fig. S11D).

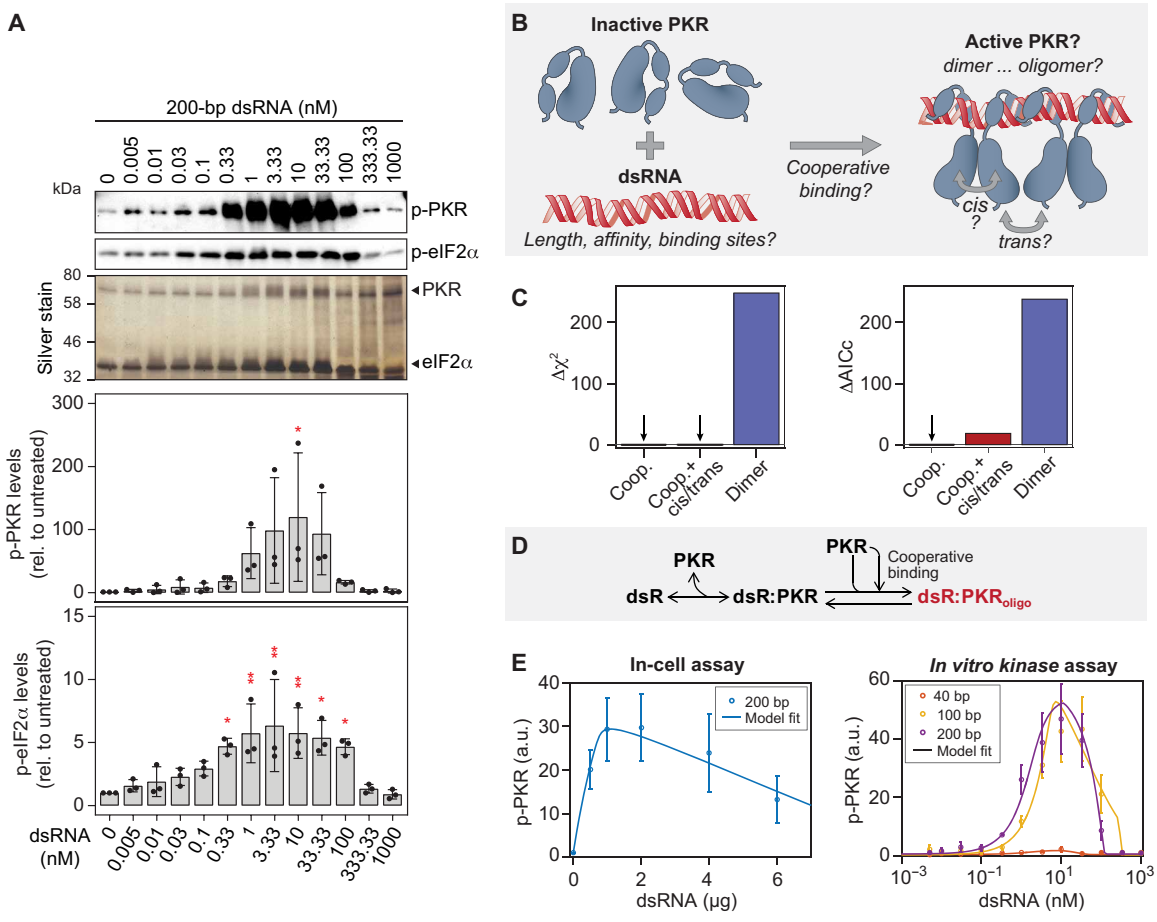

Fig. 4. Activation of PKR by dsRNA. (**A**) In vitro PKR kinase assay. His-tagged PKR and His-tagged eIF2α were incubated with increasing molarities of 200-bp dsRNA ($n = 3$). The top panels show representative Western blot analyses of p-PKR and p-eIF2α levels. Silver staining of proteins in the gel served as loading control. Quantifications of mean levels relative to untreated control ± SD are shown in the bottom panels. Statistical significance is indicated compared to untreated; $^{*}P < 0.05$, $^{**}P < 0.01$. (**B** to **E**) Computational prediction of PKR activation by dsRNA. (B) Overview of the different steps tested in PKR model development. (C) Differences in the chi-square ($\Delta\chi^2$) and corrected Akaike information criterion (ΔAICc) to the optimal PKR activation model variant (variant 3, see figs. S6 and S7). The model describing PKR dimerization upon binding to dsRNA was significantly improved by considering PKR cooperative binding to dsRNA (ΔAICc > 200). *Cis* and *trans* reactions did not improve the cooperativity model (ΔAICc = 18.4). (D) Overview of the optimal model variant. PKR monomers reversibly bind to PKR on dsRNA in a cooperative manner and form active PKR oligomers (dsR:PKRoligo). (E) Best model fits of p-PKR levels to in-cell (related to Fig. 3B) and in vitro kinase assays ($n = 500$ multistart optimization runs). a.u., arbitrary units.

Together, these results identified Huh7 cells as a unique cell system that allows studying GADD34 stress–induced transcriptional regulation independently of the induced innate immunity pathway. The GADD34 negative feedback loop presents several features that can act as sources of oscillations, e.g., a time delay caused by the need to transcribe and translate GADD34 mRNA, and nonlinear degradation of GADD34. In addition, FISH experiments pointed to an important stochasticity in the expression of GADD34 in this cell system.

Behavior of the ISR components upon stresses of varying intensities

Subsequently, we developed an integrative ODE model describing the ISR in which we combined our findings regarding kinases activation, SG formation, and the negative feedback from GADD34 to characterize the ISR functional properties. According to our experimental datasets, eight model parts describing the ISR depending on either PKR, PERK, or HRI were formulated. Model parts contained individual parameters for stress kinases and shared kinetic parameters for eIF2α (de)phosphorylation, GADD34 promoter activation, transcription, and translation. For parameter estimation, model parts were constrained to measured concentrations of eIF2α, PKR, GADD34 protein, and mRNA, and simultaneously fitted to all datasets (Fig. 5B; fig. S10 A to H; and section S4). Since the direct measurement of HCV dsRNA concentrations in infected cells was technically not possible, we extracted starting values from the live-cell imaging experiments assuming that these are proportional to the mean signal intensity of NS5A-mCherry (fig. S10I). Model equations, definitions of observables, parameter estimates, and parameter confidence intervals determined by profile likelihood estimation are provided in tables S2 to S4.

Using this parameterized ISR model, we studied the behavior of the system over a broad range of stress intensities. To this end, we predicted steady-state levels of the key species in response to a

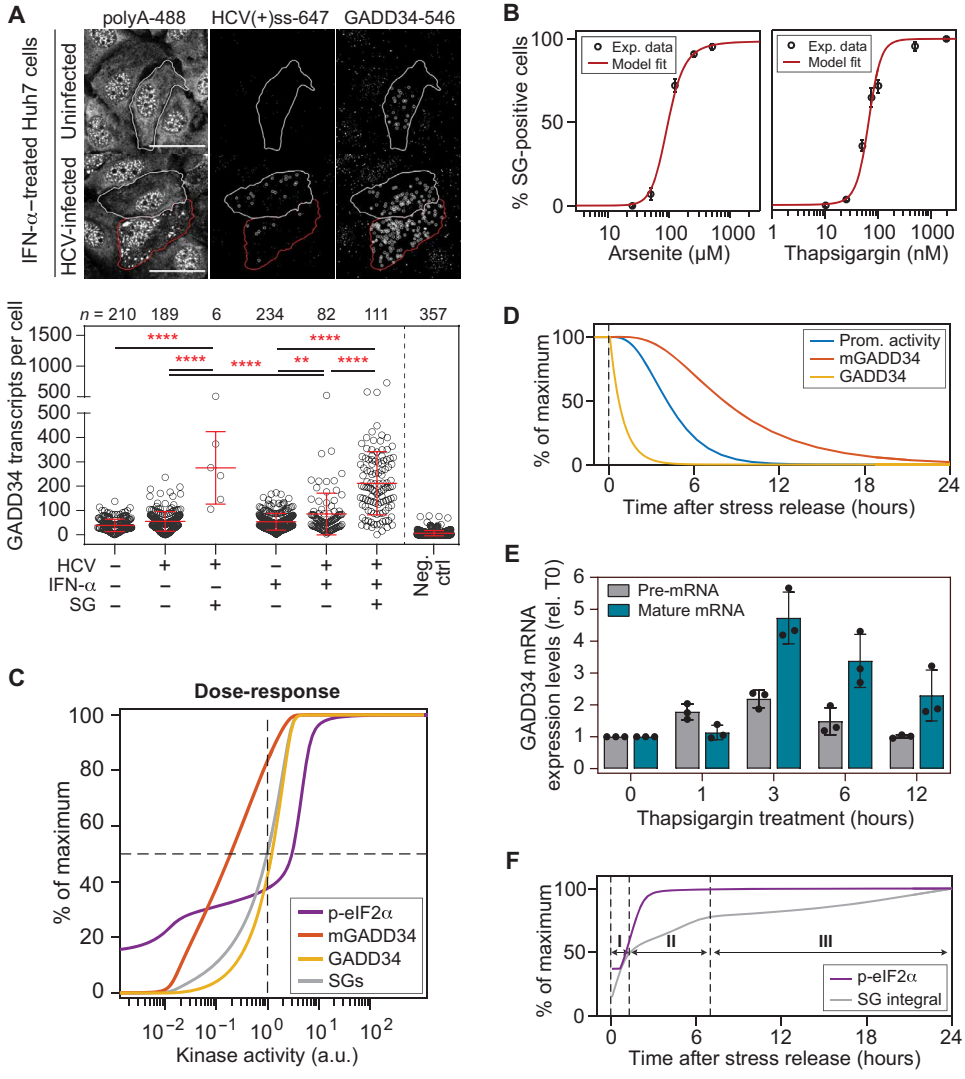

Fig. 5. Analysis of GADD34 negative feedback loop. (**A**) FISH analysis. Top: Representative still images of uninfected and HCV-infected cells treated with IFN-α. HCV (+) ssRNA genomes, GADD34 transcripts, and total polyA-tailed mRNAs were detected by FISH. Outlined in red, SG-positive cell; outlined in white, unstressed cell. White circles indicate single transcripts. Scale bars, 20 μm. Bottom: GADD34 mean transcript levels ± SD. Statistical significance and the number of analyzed cells (*n*) are indicated at the top of the graph; $^{**}P < 0.001$, $^{****}P < 0.0001$. (**B**) Model best fits ($n = 2500$ multistart optimization runs) to the percentage of SG-positive cells experimentally measured in arsenite or thapsigargin titration. (**C**) Computational simulations of dose-response curves for p-eIF2α, GADD34 mRNA, and protein and SG-positive cells in the population at steady state. Shown are percentages of maximal values as a function of different kinase activities. The reference kinase activity (10^0) results in 50% SG-positive cells (intermediate stress). Kinase activities $<10^{-1}$, low to moderate stress; >2, high stress. (**D**) Model prediction: behavior of the GADD34 negative feedback loop parameters (promoter activity, mRNA, and protein) after stress release. The percentage of their maximum response over time is shown. Estimated decay processes {$t_{1/2}$, Prom. ≈ 256 min; mRNA ≈ 200 min [from (*45*)]; protein ≈ 37 min}. (**E**) Mean expression levels ± SD of GADD34 pre-mRNA and mature mRNA upon thapsigargin treatment ($n = 3$). (**F**) Model prediction: behavior of p-eIF2α levels and number of SG-positive cells after a second 1-hour stress pulse applied at different times after stress release. Phases I to III, levels of cell protection against a second stress pulse.

1-hour stress pulse of different intensities, here reflected by different eIF2α-kinase activity levels. We defined a kinase activation level at which 50% of cells form SGs (intermediate stress) as arbitrary reference and analyzed the response to a range of activation levels, from 100-fold lower (mild stress) to 100-fold higher (acute stress) than the reference. As shown in Fig. 5C, the simulations recapitulated the ultrasensitive switch-like behavior of SG formation and GADD34 protein expression within a narrow range of kinase activity around the reference, reaching maximum levels for a twofold increase of kinase activity. In contrast, GADD34 mRNA levels were predicted to increase steadily with the kinase activity. p-eIF2α followed a biphasic dose-response curve with a largely hyposensitive phase at mild and moderate stress, during which levels increased only moderately because of the GADD34 negative feedback (between 100-fold less and 2-fold more than the reference), and a hypersensitive phase at higher stress levels (between 2- and 10-fold more than the reference) because of insufficient GADD34. At mild to moderate stress levels, the observed shift between the GADD34 mRNA and GADD34 protein dose-response curves suggested that the accumulation of mRNA allows for rapid GADD34 translation in response

to moderate p-eIF2α increases, which could be regarded as the "memory" of the previous ISR activation, possibly conferring transient adaptation to stress.

GADD34 negative feedback loop determines cell adaptation to acute and chronic stress

Adaptation in biological processes refers to the ability of a system to return to or overshoot its initial state after a transient response to environmental changes (*35*, *36*). To investigate this possibility, we simulated the levels of all components involved in the GADD34 negative feedback loop over time following a 1-hour stress pulse that leads to a maximal stress response. The promoter activity of *ppp1r15a* and the levels of GADD34 mRNA and protein all returned to basal levels upon stress release, yet with different kinetics (Fig. 5D). Because GADD34 translation is regulated by a uORF-dependent initiation step highly sensitive to p-eIF2α levels and its determined turnover was below 1 hour, GADD34 protein levels declined first, followed by *ppp1r15a* promoter activity, and, finally, GADD34 mRNA. We experimentally confirmed this prediction by measuring GADD34 premature mRNA levels, as a proxy for promoter activity, and GADD34 mature mRNA levels in cells treated with thapsigargin over 12 hours. GADD34 pre-mRNA peaked at 3 hours and returned to basal levels at 6 hours, while mature mRNA remained elevated for up to 12 hours (Fig. 5E). On the basis of this result, we delineated three time windows after stress release during which cell responsiveness to a second stress pulse increases over time according to the sequential decay of the different GADD34 species (Fig. 5F, phases I, II, and III), with phase I corresponding to a short refractory state in which responsiveness to stress is weak owing to the remaining GADD34 protein, and full responsiveness recovered after 20 hours.

To address the hypothesis of stress adaptation, we simulated consecutive acute stress pulses of varying intensity interspaced by a 5-hour recovery period. Since the duration of the kinase activity is known to influence cellular response outcome (*37*), we modeled different half-lives of kinase activity lasting up to 4 hours (Fig. 6A and fig. S12). In all scenarios, the second stress pulse resulted in highly attenuated p-eIF2α and SG responses because of the lasting *ppp1r15a* promoter activity and continued presence of high GADD34 mRNA levels (Fig. 6A). This suggests that GADD34 can be directly translated after restimulation, leading to rapid dephosphorylation of eIF2α and SG disassembly. To experimentally test this hypothesis, we subjected cells to consecutive stress pulses. Because of its rapidly reversible nature, we chose to heat shock cells for 1 hour at 42°C and allowed them to recover for 5 hours at 37°C before challenging them with a second heat pulse. As shown in Fig. 6B, the first heat pulse resulted in about 50% of p-eIF2α. Mirroring the appearance of GADD34 protein, the percentage of p-eIF2α decreased over the next 5 hours of recovery, however, without reaching its basal level. As predicted, the second heat shock did not increase p-eIF2α levels, confirming the lack of cell responsiveness to a second acute stress in this short time window. Together, using the calibrated model, we predicted and experimentally validated that the sustained presence of GADD34 mRNA and GADD34 protein limits or prevents the response to the second stress.

Different from arsenite, thapsigargin, or heat shock, stress induced by chronic HCV infection is continuous and probably of milder intensity. In addition, by the time cells are treated with IFN-α (48 hours after infection), viral replication has reached a steady state (fig. S1A). We thus predicted the behavior of the SG response under continuous stress of different intensities over a period of 24 hours (Fig. 6C). Moderate to intermediate stress resulted in a single burst of eIF2α phosphorylation and SG assembly, and the response declined as a function of GADD34 mRNA and protein induction. In the following, the GADD34 mRNA levels showed a slight decrease after 8 to 10 hours for the milder stress but remained at a higher plateau compared to the initial level in all cases. This was similar for the level of p-eIF2α and the fraction of SG-positive cells in the population. These predictions explain our previous results, where we observed that the percentage of HCV-infected cells displaying SGs reached a plateau of 30 to 40% within 12 hours of IFN-α treatment, accompanied by the expression of high GADD34 mRNA levels when measured in bulk (*11*). Together, this result strongly suggests that under infection-induced stress conditions, sustained levels of GADD34 mRNA and protein promote long-term cell adaptation to stress.

To test more accurately whether such an adaptation scenario occurs during HCV infection, we simulated the levels of p-eIF2α and SG-positive cells at 1, 3, and 12 hours after stress using the range of PKR activities determined experimentally in untreated and IFN-α–treated Huh7 cells (Fig. 6D). At the low to moderate levels of PKR activation achieved in untreated HCV-infected cells, cells were predicted to rapidly adapt within 3 hours of the onset of stress, going from 100% SG-positive cells within 1 hour to less than 25% within 3 hours, an amount that did not change after 12 hours. In contrast, at intermediate levels of PKR activation in the presence of IFN-α, adaptation was expected to be slower, with approximately 75% of SG-positive cells after 3 hours and 50% after 12 hours before reaching a steady state. The analysis of experimental single-cell SG response time series supported this hypothesis and revealed the rapid appearance of SGs in most cells after IFN-α addition. This first SG-On phase was long (approximately 12 hours), followed by shorter phases (see Fig. 1C). This suggested that, in our system, HCV infection can be considered as a first stressor, amplified by the addition of IFN-α that up-regulates PKR, after which cells slowly adapt to stress and exhibit shorter SG phases.

In conclusion, our quantitative deterministic model comprehensively describes the main components of the cellular ISR and temporal behavior of the SG response at steady state. Moreover, our results revealed an unexpected function of GADD34 mRNA levels as a molecular memory of the system, which promotes adaptation of cells under mild stress conditions after an acute stress.

A fine-tuned balance between PKR and dsRNA levels determines SG response dynamics

Although the ISR signaling network could theoretically support sustained oscillations because of the existence of a time delay resulting from GADD34 transcriptional and translational activation (*12*, *22*, *27*), the deterministic approach described above was not sufficient to explain the experimentally observed SG response dynamics with recurrent cycles of SG formation. This implied that additional stochastic processes regulate HCV-induced SG response dynamics. We hypothesized that the heterogeneity observed in the SG time series could be influenced by additional aspects, including (i) the inherent stochasticity in GADD34 and PKR expression whose initial protein abundance is low (*17*, *38*, *39*); (ii) the inherent stochasticity of the infection process, as the number of particles entering a cell depends on a probabilistic process (*40*); and (iii) the presence of IFN-α, which induces antiviral proteins, including PKR, and represses HCV replication over time (see fig. S1B). To assess these possibilities, we

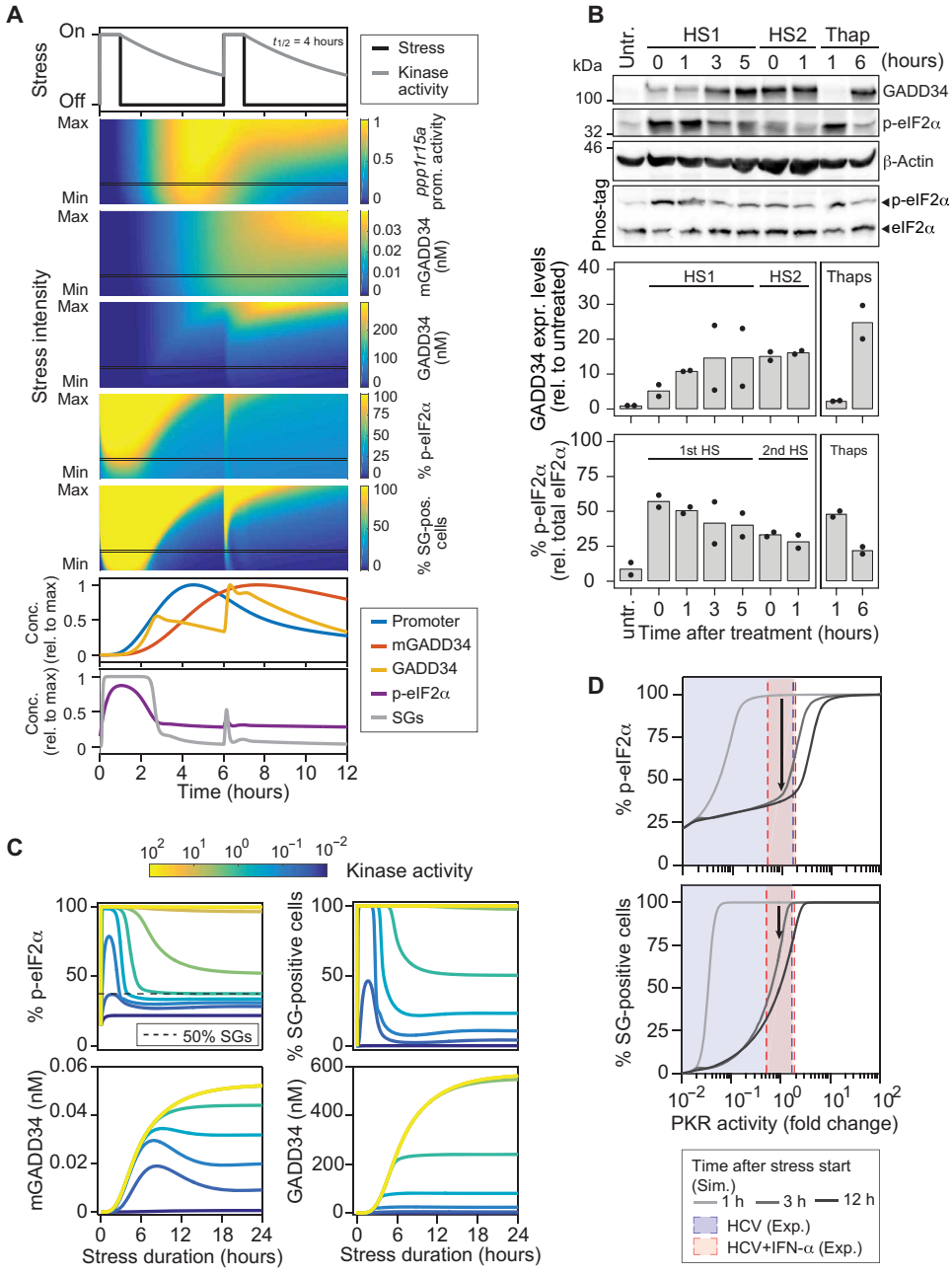

Fig. 6. Cell adaptation to repeated and continuous stress. (**A**) Computational simulations of two consecutive 1-hour stress pulses interspaced by a 5-hour recovery period. Shown is a range of stress kinase activities (stress intensity) varying between 10-fold lower (min) and 10-fold higher (max) than the reference kinase activity leading to 50% SG-positive cells. Color plots show the behavior of *ppp1r15a* promoter activity, concentrations of GADD34 mRNA and protein, and percentages of p-eIF2α and SG-positive cells. Graphs at the bottom reflect the behavior of the abovementioned components for one chosen stress intensity (black line, moderate stress). (**B**) Experimental validation of the predictions shown in (A). Huh7 cells were subjected to a first heat shock (HS1) at 42°C for 1 hour and immediately transferred at 37°C for recovery. Cells were harvested at the indicated time points after the first or the second heat shock (HS2) ($n = 2$). Cells treated with 2 μM thapsigargin for 1 and 6 hours served as reference. Shown are representative Western blot and Phos-tag gel analyses. Bottom panels show the quantification of GADD34 expression levels normalized to the loading control and relative to untreated cells as well as the percentage of p-eIF2α. (**C**) Model prediction: behavior of the SG response and GADD34 negative feedback loop components over a 24-hour time period upon continuous stress. The color of the curves reflects different kinase activity levels. (**D**) During the adaptation to a stress stimulus, depending on PKR activity, the expression of GADD34 will result in dose-response curve shifts (hysteresis) in the percentage of p-eIF2α (top) and of SG-positive cells (bottom). The shift of the dose-response curve depends on the stress duration and intensity and is reverted after stress relief. Blue and red shared areas indicate 1σ confidence intervals of estimated PKR activities in HCV and HCV + IFN-α experiments.

translated the calibrated ODEs into a corresponding stochastic model describing reactions downstream of PKR activation. To this end, kinetic parameters were transformed into reaction propensities. First, to account for the heterogeneity of our cell system as closely as possible, we analyzed the cell-to-cell variability of eIF2α and PKR by single-cell Western blot analysis (fig. S13, A to D) (*41*). Individual Huh7 cells were loaded into the microwells of array slides patterned in a photoactive polyacrylamide gel. After chemical lysis, electrophoresis, and ultraviolet (UV) fixation, proteins were stained with primary and fluorescently labeled secondary antibodies. The presence of cells in wells was confirmed by staining with glyceraldehyde-3-phosphate dehydrogenase (GAPDH). For PKR detection, Huh7 PKR_{KO} cells were used as background control. Within the population of Huh7 cells, signal intensities varied by more than fivefold for eIF2α (fig. S13, A and B), threefold for PKR, and by more than sixfold for PKR in cells treated with IFN-α (fig. S13, C and D). We combined these results with the previously determined mean concentrations and thereby determined the log-normal distribution of PKR and eIF2α initial values to be implemented in the model (section S5). In addition, parameters for the log-normal distribution of NS5A-mCherry intensity were calculated from the live-cell imaging data (fig. S13E and section S5).

To simulate the ISR in a heterogeneous cell population, concentrations of PKR, eIF2α, and infection levels were sampled and used as initial conditions for stochastic simulations of single-cell SG response time series (Fig. 7A). The time series as well as the distribution in SG phase number (Fig. 7B) and stress duration (integral of stress) per day (Fig. 7C) closely reflected the experimental results obtained in live-cell imaging, especially for IFN-α–treated cells.

Next, we used the stochastic model to systematically characterize the behavior of the system over a broad range of PKR and dsRNA concentrations. The dsRNA concentration, serving as input for stochastic simulations, was scaled relative to the level analyzed experimentally in HCV-infected cells in the absence of IFN-α treatment, corresponding to maximum HCV levels. Color plots in Fig. 7 indicate the number of SG phases and stress duration per day (Fig. 7, D and E), as well as the levels of active PKR (Fig. 7F) obtained from simulations of 500 SG response time series per condition. Results revealed that highly fluctuating SG responses occurred only in a narrow range of dsRNA concentrations of about one-third of the reference level (Fig. 7D), consistent with the concentration experimentally determined in HCV-infected cells treated with IFN-α (Fig. 7D, pink dot and surrounding area). This prediction also postulated a critical PKR concentration of approximately 25 nM as a threshold below which PKR is not activated in Huh7 cells, regardless of the dsRNA concentration. In agreement with this, we experimentally observed that about half of the Huh7 cells in the population had PKR concentrations below this level, thus accounting for the reduced responsiveness of the population and reduced number of SG phases per day observed in HCV-infected cells. The PKR concentration increases upon treatment with IFN-α, bringing the cells into a state that allows for dynamic SG responses. Furthermore, the simulations revealed that concentrations of dsRNA threefold higher than the reference would result in a loss of SG response dynamics, as reflected by the decrease of the number of SG phases per day and an increase in the stress duration, suggesting that SG-On phases would become longer up to reaching a plateau of permanent stress response (Fig. 7E).

Last, we decided to perturb the system and predict the impact of higher PKR levels on SG response dynamics in HCV-infected cells. Key SG component concentrations in Huh7 cells stably overexpressing PKR (PKR_{OE}) (*11*) were experimentally determined as previously done for naïve Huh7 cells (fig. S14, A and B). Huh7 PKR_{OE} cells expressed mean PKR levels approximately 8.3-fold higher than Huh7 cells and 2.7-fold higher than Huh7 cells treated with IFN-α. Ectopic PKR expression did not affect eIF2α expression levels. In addition, cell-to-cell variability was determined by single-cell Western blot (fig. S14, C and D). Last, cell-to-cell variability in GADD34 transcripts was analyzed by FISH (fig. S14E). These experimentally determined distributions were used as input for the stochastic model to simulate the SG response when PKR is overexpressed. The resulting time series predicted distinct SG response dynamics with longer SG-On phases that were only rarely interspersed with SG-Off phases (Fig. 7A, model simulations HCV + PKR_{OE}). To experimentally test this prediction, Huh7 PKR_{OE} cells were infected with HCV_{TCP} for 48 hours, and SG formation was monitored using live-cell imaging for an additional 72 hours (Fig. 7A, Exp. HCV + PKR_{OE}, and movie S3). The analysis of the experimental single-cell SG response time series showed that, as predicted by the model, cells displayed on average longer SG-On phases and a higher stress duration per day (Fig. 7, C and E, HCV + PKR_{OE}). Consistently, this was paralleled by a reduced number of SG phases per day (Fig. 7, B and D, HCV + PKR_{OE}).

Collectively, our results revealed that the dynamic SG response to HCV infection and, generally, to dsRNA consists of repetitive stochastic transitions between On and Off states that are regulated by PKR and dsRNA concentrations in individual cells. The stochastic version of the deterministic model that was calibrated using an extensive experimental dataset could successfully predict characteristics of single-cell SG responses in heterogeneous cell populations and was independently validated for the case of PKR overexpression. In addition, our modeling approach points toward elevated GADD34 mRNA expression levels that act as a memory of previous ISR activation and enable long-term adaptation of chronically infected cells to the continuous presence of virus.

DISCUSSION

The ISR is a pivotal process that allows cells to adapt to environmental changes by rapidly repressing host cell translation, thereby preventing damage to nascent polypeptides and reallocating resources to restore homeostasis. Its regulation has been the subject of many studies involving mathematical modeling (*31*, *42*–*47*). However, these studies have mainly focused on the unfolded protein response (UPR) network via PERK-eIF2α signaling. Possible periodic oscillations of the stress response components were predicted in only two of the studies under certain parameter conditions that were not determined quantitatively (*31*, *47*). While these studies provided valuable information on the possible behavior of the stress response over time, they could not explain the peculiar SG fluctuations observed in response to chronic HCV infection.

By combining long-term live-cell imaging, population and single-cell analyses, and ODE modeling, we here provide a detailed quantitative insight into the individual regulatory steps of the ISR, including SG formation. In particular, we captured the dynamics and role of the different components of the stress response to HCV infection. In the quantitative model we developed, eIF2α is the central reaction component of the system whose phosphorylation mediated by the different eIF2α kinases can be reversed by PP1 in

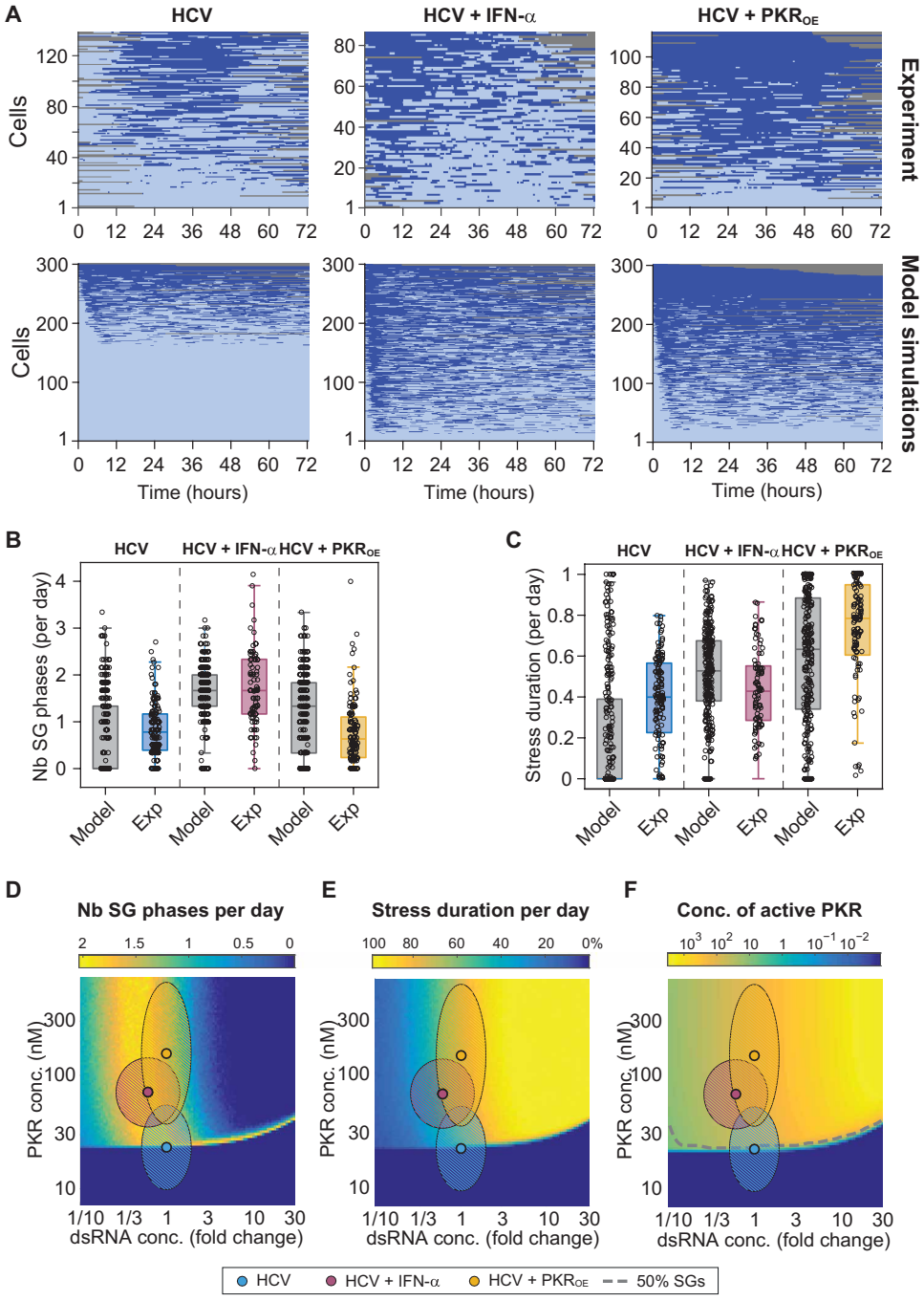

Fig. 7. Stochastic mathematical model of the ISR recapitulates HCV-induced SG response dynamics. (**A** to **C**) Comparison of experimental and computational simulations of 3-day single-cell SG response time series using the parameters estimated in HCV-infected cells in the presence and absence of IFN-α, and in HCV-infected Huh7 PKR_{OE} cells (bottom, $n = 300$) (A). Corresponding number of SG phases per day (B) and stress duration per day (C) were compared. Boxes indicate 25th and 75th percentiles around the median. (**D** to **F**) Computational simulations of average SG phases per day (D), stress duration per day (E), and concentration of active PKR (F) for varying PKR and dsRNA concentrations. DsRNA concentrations are expressed as fold changes relative to conditions of the HCV experiment (simulations of 500 single-cell trajectories per combination; hatched ellipsoid areas: 95% confidence intervals for HCV and HCV + IFN-α experiments).

complex with GADD34 in a negative feedback manner. Although the topology of this stress-kinase-eIF2α-GADD34 signaling network displays the hallmarks of a biological oscillator (*12*), and despite our previous intuitive description of HCV-induced SG-On and -Off phases as "oscillations," the Fourier transform analysis of hundreds of single-cell SG response time series suggested that the observed SG phases are rather bursts controlled by a stochastic process with memory. While our mathematical analysis focused on finding distinct oscillation frequencies in a heterogeneous cell population, we cannot exclude the existence of individual cells whose parameters

may lie in the range that permits oscillation. An algorithm developed by Phillips and colleagues represents an attractive alternative that allows finding single oscillators of varying frequencies in a cell population, thereby differentiating between signal fluctuations and noise (*48*). However, the binary SG response time series generated by our analysis pipeline are not suitable for this type of analysis, which requires a continuous signal as well as a signal amplitude as input information.

Dose-response experiments with arsenite and thapsigargin treatments provided evidence for the remarkable switch-like behavior of SG formation. This was reflected by a steep sigmoidal response curve and high Hill coefficients and suggested that SG assembly is a highly cooperative process, consistent with current knowledge about SG assembly by liquid-liquid phase separation (*49*). Thus, we determined a threshold level of p-eIF2α of 38% (arsenite) and 30% (thapsigargin), which is critical for Huh7 cells to switch to an SG-On phase. These values depend on the concentration of the respective kinase and are in the range of what other studies described (*50*–*52*).

Some aspects of the mechanism of PKR activation are still unclear, including how monomers are recruited to dsRNA. By combining the quantitative information on the stoichiometry of PKR activation obtained in vitro and mathematical modeling, we observed cooperative binding of PKR molecules to 100- and 200-bp dsRNA, unlike what others have seen to shorter dsRNAs (*8*). Regardless of dsRNA length, maximal PKR activation and eIF2α phosphorylation were achieved at 10 nM dsRNA, a concentration lower than previously reported (*8*, *53*), which might be explained by lower concentrations of PKR and salt in our assay. Unlike what is observed at higher concentrations (*54*), our results did not provide evidence that at the physiological level, PKR can be activated in the absence of dsRNA. Because of the absence of time-resolved measurements, the previously hypothesized contribution of *cis* (intramolecular) and *trans* (intermolecular) interactions in PKR activation was not evident from our dataset (*25*, *26*, *54*–*56*). In the context of virus-infected cells, PKR activation remains enigmatic. The fact that HCV, like many RNA viruses (*57*), replicates in specialized compartments derived from ER membranes, presumably to protect its genome from cytosolic innate immune sensors, raises the question of the accessibility of PKR to dsRNA replication intermediates.

An important finding of our deterministic model was that the ISR allows different levels of adaptation. Adaptive responses have been reported for various biological systems, e.g., during osmotic shock in yeast (*58*), perturbations of calcium homeostasis in mammalian cells (*59*), and chemotaxis in *Escherichia coli* (*60*). Adaptation is defined, from a biochemical point of view, as the ability of a system to respond to a stimulus and return to the prestimulus state or to a different steady state. In this manner, cells can maintain homeostasis, especially in the presence of persistent perturbations (*61*). The topology of our ISR model exhibits strong similarity with other theoretical minimal networks, e.g., the negative feedback loop with a buffer node (*35*), previously described to allow biochemical adaptation. Although theoretically possible, our deterministic model of the ISR revealed the absence of oscillations (for p-eIF2α level and SG response) within the experimentally determined range of the different parameters. Using repeated heat pulses, we confirmed that after a first acute stress, long-lasting GADD34 mRNA levels protect cells from responding to a second stress pulse. For a continuous stress of intermediate intensity, as triggered by HCV infection in the presence of IFN-α, our analyses confirmed that adaptation occurs within 12 hours, with GADD34 mRNA levels remaining at a high steady-state level over time (*11*). On the basis of this result, we propose that GADD34 transcriptional activation and mRNA serve as a memory of the system, allowing for rapid GADD34 translation and limiting the SG phase duration in the case of both acute and continuous stress. Our results are in agreement with several studies that have either addressed the impact of repeated stress pulses theoretically (*42*, *43*) or explored the response of chronic chemical stress experimentally (*44*, *46*, *62*). It is therefore tempting to speculate that a strong activation of the ISR, resulting in high steady-state levels of GADD34, might be beneficial to acute viruses.

Last, our work highlights the importance of cell-to-cell variability and stochasticity in shaping cellular responses to stress. Translating the calibrated model into a corresponding stochastic model, by taking into account random bursts of transcription and cell-to-cell variability, allowed us to faithfully model HCV-induced SG response fluctuations observed in long-term live-cell time lapses. To our surprise, the results indicated that recurrent SG phases occur only in a relative narrow range of PKR and dsRNA concentrations. By combining the information obtained from the calibrated deterministic and stochastic models, we propose a scenario in which the stress response to HCV infection, in the presence of IFN-α, reaches a steady-state level within 12 hours, determined by the concentration of active PKR and dsRNA at the single-cell level, allowing for an adaptation to this type of viral chronic stress. In this system, recurring SG-On and SG-Off phases are caused by stochastic events that perturb the steady-state level of eIF2α phosphorylation and evoke bursts of GADD34 transcription.

In our quantitative hybrid model of the ISR, the fact that the eIF2α kinases share a common downstream signaling pathway opens up several possibilities for future investigations. For instance, it will be interesting to investigate the impact of sustained ISR activation by other chronic treatments with low doses of chemical stress inducers or, conversely, by acute viruses, and thus include information on cell survival. Likewise, it would be interesting to consider in the model that viruses often interfere simultaneously with other branches of the UPR (*5*). This may influence the return of cells to homeostasis and the decision between adaptation, survival, or cell death programs. Last, expanding the model to quantitative datasets from IFN-competent cell types and other RNA viruses would further shed light on the role of the IFN-mediated regulation of GADD34 expression in the ISR to virus infection. Together, the hybrid model developed here will help to further understand the detailed mechanisms and kinetics underlying cellular adaptation to stress and stress recovery.

MATERIALS AND METHODS

Cell lines and media

All cell lines were cultured in Dulbeccos's modified Eagle's medium (DMEM) supplemented with 2 mM L-glutamine, 1× nonessential amino acids, penicillin (100 U/ml), streptomycin (100 μg/ml) (GIBCO), and 10% fetal calf serum (FCS) (Capricorn), hereafter referred to as DMEM complete. Human embryonic kidney (HEK) 293T cells were used for lentivirus particle production. Huh7 PKR_{KO} clones were described elsewhere (*63*). Huh7 YFP-TIA1 Neo cells (*11*) were supplemented with G418 (1 mg/ml; Life Technologies). Huh7 YFP-TIA1 Neo PKR Blr cells and Huh7 PKR Blr cells (PKR_{OE}) (*11*) were supplemented with blasticidine (5 μg/ml; Life Technologies). Huh7 GADD34 Puro cells (*11*) were supplemented with puromycin (3 μg/ml;

Sigma-Aldrich). Huh7.5 cells (*64*) were used for production of HCV (Jc1) virus stock. Huh7.5 [CE1][E2p7NS2] Blr cells (*65*) were supplemented with blasticidine (5 μg/ml) and used for the production of HCV_{TCP}. For live-cell microscopy, cells were maintained in phenol red–free DMEM containing 1 mM Hepes, penicillin-streptomycin, and 10% FCS.

Plasmids

A plasmid encoding HCV subgenomic replicon harboring *Renilla* luciferase (RLuc) and mCherry fused to HCV NS5A was generated by Pme I and Age I digest of pFKI389neoNS3-3'dg_JFH-1_NS5A-aa383_mCherry K1402Q plasmid (*11*). RLuc coding sequence flanked by Age I and Pme I restriction sites was amplified from the vector pFK i389 JcR2a dg (*66*) by polymerase chain reaction (PCR) using Phusion High-Fidelity DNA polymerase (New England Biolabs) using the following primers: Age I-RLuc_For: 5′-CGGAACCGGTGAGTACAC-3′ and RLuc-Pme I_Rev: 5′-AGGCGTTTAAACTTATTCATTTTTGAGAACTCG-3′. This replicon (pFKI389RLuc_NS3-3′dg_JFH-1_NS5A-aa383_mCherry K1402Q) was designated "HCV RLuc-mCherry replicon".

To generate plasmids used for bacterial expression of recombinant His-tagged proteins, sequences of *EIF2AK2* and *EIF2S1* were amplified by PCR using the Phusion Flash High-Fidelity PCR Master Mix (Thermo Fisher Scientific), pWPI PKR Blr or pET-MCN eIF2α as template, and primers introducing sequences C- and N-terminally overlapping with the pET-His 1a vector (PKR_For: 5′-TTATTTTCAGGGCGCCATGGCTGGTGATCTTTCAG-3′ and PKR_Rev: 5′-CGAATTCGGATCCGGTACCCTAACATGTGTGTCGTTC-3′; eIF2α_For: 5′-TTATTTTCAGGGCGCCATGCCGGGTCTAAGTTGTAG-3′ and eIF2α_Rev: 5′-CGAATTCGGATCCGGTACCTTAATCTTCAGCTTTGGCTTC-3′). Full pET-His 1a vector was amplified by PCR (pET-His_1a_For: 5′-GGTACCGGATCCGAATTCG-3′ and pET-His_1a_Rev: 5′-GGCGCCCTGAAAATAAAG-3′) using the following conditions: 98°C for 10 s and 30 cycles of 98°C for 1 s, 55°C for 5 s, and 72°C for varying periods (90 s for PKR, 15 s for eIF2α, and 20 s for pET-His 1a). A final extension at 72°C for 60 s was performed. Template plasmid was digested using FastDigest Dpn I (Thermo Fisher Scientific) for 1 hour at 37°C. PCR products were purified from agarose gels using the Nucleospin Gel and PCR Clean-Up kit (Macherey-Nagel). *EIF2AK2* and *EIF2S1* sequences were inserted into pET-His 1a vector using the Gibson Assembly Cloning Kit (New England Biolabs) as described by the manufacturer.

pWPI GADD34-$(G_4S)_4$-eGFP Puro used for absolute quantification of GADD34 molecules per cell was generated by amplifying *ppp1r15a* sequence from its cDNA clone (*11*) by PCR using the following primers: Xho I_GADD34_For: 5′-AACTTCCTCGAGATGGCCCCAGGCCAAGCACCCCATC-3′ and Hind III_GADD34_Rev: 5′-GGATCGAAGCTTGCCACGCCTCCCACTGAGGTCCAGG-3′. First, the PCR product and vector pTurboGFP-N (Evrogen) were digested with Xho I and Hind III, purified, and ligated to generate pGADD34-TurboGFP. Second, the sequence of a $(G_4S)_4$-linker flanked by Hind III and Age I restriction sites was generated by hybridizing 100 μM of each of the following oligonucleotides [Hind III_$(G_4S)_4$_Age I_For: 5′-AGCTTGGTGGAGGCGGGTCTGGGGGCGGAGGTTCAGGCGGGGGTGGTTCCGGTGGCGGTGGCTCGGGA-3′ and Age I_$(G_4S)_4$_Hind III_Rev: 5′-CCGGTCCCGAGCCACCGCCACCGGAACCACCCCCGCCTGAACCTCCGCCCCCAGACCCGCCTCCACCA-3′] in annealing buffer [25 mM Hepes (pH 7.4) and 50 mM NaCl] at 95°C for 5 min followed by a gradual decrease in temperature to 25°C at 5°C/min. Hybridized oligonucleotides were phosphorylated with 5 U T4 polynucleotide kinase in T4 Ligation Buffer (New England Biolabs) for 30 min at 37°C. Last, pGADD34-TurboGFP was digested by Hind III and Age I, and pGADD34-$(G_4S)_4$-TurboGFP was generated by ligation with the hybridized oligonucleotide. Of note, TurboGFP was exchanged for eGFP by amplifying the eGFP sequence by PCR from peGFP-N1 (Clontech) using the following primers to introduce Age I and Not I restriction sites: Age I_eGFP_For: 5′-TTATTAGACCGGTCATGGTGAGCAAGGGCGAGGA-3′ and Not I_eGFP_Rev: 5′-TAATTGCGGCCGCTTACTTGTACAGCTCGTCCA-3′. PCR product and vector were digested with Age I and Not I. pGADD34-$(G_4S)_4$-eGFP was generated by ligation. GADD34-$(G_4S)_4$-eGFP sequence was finally cloned into a lentiviral vector pWPI Puro. To this end, pGADD34-$(G_4S)_4$-eGFP was digested by Xho I and Not I. The sticky end product was blunted using 10 U of DNA Polymerase I Large (Klenow) Fragment (New England Biolabs). pWPI Puro was digested by Pme I and dephosphorylated using 20 U of calf alkaline phosphatase (New England Biolabs) for 1 hour at 37°C. The lentiviral vector pWPI GADD34-$(G_4S)_4$-eGFP Puro was generated by ligation.

In vitro transcription

In vitro transcription reaction was performed as described earlier (*11*). Ten micrograms of plasmid template was linearized by restriction with Mlu I (New England Biolabs) and purified using the Nucleospin Gel and PCR Clean-Up kit (Macherey-Nagel). In vitro transcription reaction was carried out in a final volume of 100 μl of transcription mix containing 80 mM Hepes (pH 7.5), 12 mM $MgCl_2$, 2 mM spermidine, 40 mM dithiothreitol (DTT), 3.125 mM of each nucleoside triphosphate (Roche), 100 U of RNasin ribonuclease inhibitor (Promega), and 80 U T7 RNA polymerase (Promega). After 2 hours of incubation at 37°C, 40 U of T7 RNA polymerase was added to the reaction mix and incubated for an additional 2 hours at 37°C. Transcription was terminated by addition of 10 U RQ1 ribonuclease (RNase)–free deoxyribonuclease (DNase) (Promega) and incubation at 37°C for 30 min. RNA was extracted with acidic phenol and chloroform, precipitated with isopropanol, and dissolved in RNase-free water. RNA integrity was determined on nondenaturing agarose gel and concentration by measuring absorbance at 260 nm.

Analysis of HCV RLuc-mCherry replication kinetics

Huh7.5 cells were washed twice with phosphate-buffered saline (PBS) and resuspended in cytomix solution pH 7.6 [120 mM KCl, 0.15 mM $CaCl_2$,10 mM K_2HPO_4/KH_2PO_4 (pH 7.6), 25 mM Hepes, 2 mM EGTA, and 5 mM $MgCl_2$] freshly supplemented with 5 mM glutathione and 2 mM adenosine triphosphate (ATP) to a final concentration of 1.5×10^7 cells/ml. Cell suspension (400 μl) was mixed with 10 μg of in vitro transcript, transferred in a 0.4-cm electroporation cuvette (Bio-Rad), and pulsed at 975 μF and 270 V using a Gene Pulser system (Bio-Rad). Electroporated cells were immediately resuspended in 15 ml of DMEM complete and seeded into one six-well plate in duplicates. At 4, 24, 48, 72, and 96 hours, cells were washed once with PBS and lysed using 250 μl of ice-cold Luciferase Lysis Buffer [25 mM glycylglycine (pH 7.8), 15 mM $MgSO_4$, 15 mM K_2PO_4, 4 mM EGTA, 10% (v/v) glycerol, and 0.1% Triton X-100] freshly supplemented with 1 mM DTT. Samples were stored at −80°C. *Renilla* luciferase activity in cell lysates (20 μl) was

measured with 100 µl of Luciferase Assay Buffer [25 mM glycylglycine (pH 7.8), 15 mM $MgSO_4$, 15 mM K_2PO_4, and 4 mM EGTA] in duplicates using the tube luminometer LB9507 (Berthold Technologies). Relative light unit (RLU) values from the 4-hour time point after electroporation served as input control for normalization.

Virus production and titration

RLuc-mCherry HCV_{TCP} was used to observe SG response dynamics by live-cell imaging. Huh7.5 [CE1][E2p7NS2] Blr cells were electroporated with 10 µg of HCV RLuc-mCherry replicon in vitro transcript as described above, immediately resuspended into 6.5 ml of DMEM complete, and seeded into a 10-cm cell culture dish. Virus supernatants were collected at 24, 48, 72, and 96 hours after electroporation, filtered through a 0.45-µm-pore size membrane (Merck), and stored at −80°C.

Full-length HCV Jc1 was used to analyze levels of various proteins and transcripts per cell during virus infection. Huh7.5 cells were electroporated with in vitro transcripts from pFK-J6/C3 (*67*) and processed as described above. Virus supernatants were concentrated by precipitation using 8% (w/v) polyethylene glycol-8000 in PBS for 72 hours at 4°C followed by centrifugation at 8000*g* for 2 hours at 4°C. The virus pellet was resuspended in DMEM complete and stored at −80°C. Infectious titers were determined by limiting dilution assay [tissue culture infectious dose 50 ($TCID_{50}$)] as described in (*68*).

Analysis of HCV_{TCP} replication kinetics upon IFN-α treatment

Huh7 cells (3×10^4) were seeded in 12-well plates and infected with HCV_{TCP} at a multiplicity of infection (MOI) of 2 $TCID_{50}$ per cell in duplicate wells for 48 hours. Medium was replaced with 2 ml of DMEM complete with and without 100 IU/ml IFN-α (PBL International). Cells were lysed at 24, 48, or 72 hours after treatment. *Renilla* luciferase activity was measured as described above. RLU values were normalized to the time point 0 of IFN-α addition.

Long-term live-cell imaging of HCV-infected cells and microscope equipment

Huh7 YFP-TIA1 Neo cells (1.8×10^4) with or without stable overexpression of PKR were seeded 24 hours before infection in 12-well plates with glass bottom (thickness 0.16 to 0.19 mm) (Cellvis). Cells were infected with HCV_{TCP} at an MOI of 1.5 $TCID_{50}$ per cell. Medium was replenished 24 hours after infection. Forty-eight hours after infection, culture medium was replenished with phenol red–free microscopy medium supplemented with IFN-α (100 IU/ml; PBL International) and transferred to the heating chamber of the microscope (Okolab). Image acquisition was performed using a Nikon Eclipse Ti2/Andor Revolution CSU-W1 spinning disc confocal microscope equipped with a 20× air objective CFI Plan Apo lambda [numerical aperture (NA) = 0.75], Nikon Perfect Focus System, Andor lasers 514 nm (40 mW) and 561 nm (50 mW), triple line dichroic beamsplitter 445/514/561, emission filters for YFP (540/30) and mCherry (600/50), Nikon motorized stage with linear encoder, electron multiplying charge-coupled device (EMCCD) Camera iXon DU-888—13 µm by 13 µm pixel size (Andor), and NIS Elements AR software (Nikon). Images (signals of YFP-TIA1 and NS5A-mCherry) were acquired in 15-min intervals for 72 hours, starting 4 to 5 hours after treatment with IFN-α. Typically, 15 to 30 fields of view were manually selected using the NS5A-mCherry signal and acquired simultaneously.

Image analysis of SG single-cell time series

Images were exported as one 16-bit hyperstack TIFF (tagged Image File Format) per field of view using NIS Elements AR software. Using the ilastik (Linux v1.3) (*20*) image conversion tool, the images were further converted into 8-bit .h5 format. The ilastik pixel classification tool was used for automatic detection of single cells, SGs, and virus protein. Random frames were used for software training by manually creating separate labels for pixels representing nuclei, SGs, background pixels (all in the YFP-TIA1 channel), and virus protein (NS5A-mCherry channel). Using the segmentation tool, segmentation masks were created for each label. Single-cell tracks were generated with the Ilastik tracking toolkit using the nuclei segmentation masks. To assign density and count as well as virus protein levels to individual cell tracks at any given point in time, we used a Voronoi partitioning of each time frame based on the nuclei segmentation center of mass. For each cell track and frame, the respective Voronoi cells were overlaid with SG and infection marker masks to generate time-resolved single-cell trajectories of total number of SG pixels, SGs, and NS5A-mCherry pixels. To exclude faulty cell tracks and SG detection, each track was manually curated using a Python/Kivy-based graphical interface iterating every time frame of long tracks (minimum length of 48 hours) and comparing time-lapse data with assigned center of mass of tracks and detected SG pixel number. Only tracks with correctly assigned presence of SGs (SG pixel threshold >15) with maximum aberrations of one frame false-positive/negative SG detection were accepted. In a further downstream data filter, all stress events/stress disruption events of one frame length were smoothed out.

Estimation of Huh7 cell volume

Huh7 YFP-TIA1 cells (10^5) were seeded in a 35-mm dish with 20-mm cover glass no. 1.5 (MatTek). Confocal Z-stacks (200 nm Z spacing) of whole cells were acquired using the YFP-TIA1 signal (514 nm excitation) on a Nikon Ti Eclipse using an Apo total internal reflection fluorescence (TIRF) 60× oil (NA 1.49) objective (Nikon) with a digital image using the Orca Flash 4 v2 camera (6.5 × 6.5 µm pixel size, Hamamatsu). Substacks with 1-µm Z spacing including the whole cell volume were chosen and manually circled to measure area per stack. Total cell volume was calculated by multiplication of total area volume with 1-µm stack thickness.

Western blot analysis

Cells were detached by trypsinization and pellets were lysed with ice-cold protein lysis buffer [50 mM tris-HCl (pH 7.3), 150 mM NaCl, 1% Triton X-100 supplemented with EDTA-free protease inhibitor cocktail (Roche), 60 mM β-glycerophosphate, 15 mM 4-nitrophenylphosphate, 1 mM sodium orthovanadate, and 1 mM sodium fluoride] on ice for 30 min. Cell debris were pelleted by centrifugation for 30 min at 13,000 rpm at 4°C. Total protein concentration was determined by colorimetric measurement using Protein Assay Dye Reagent (Bio-Rad). Bovine serum albumin (BSA, Thermo Fisher Scientific) dilutions served as protein standard for calibration. Equal amounts of total protein (20 to 100 µg, depending on experiment) were resuspended in 1× Laemmli sample buffer [62.5 mM tris-HCl (pH 6.8), 10% glycerol, 1.5% SDS, 1.5% β-mercaptoethanol, and 0.01% bromophenol blue], denatured for 5 min at 95°C, separated by SDS–polyacrylamide gel electrophoresis (SDS-PAGE), and transferred to a polyvinylidene difluoride membrane (Millipore). Membranes were blocked by incubation with tris-buffered saline

containing 0.1% Tween 20 and 5% (w/v) skim milk powder or 5% (w/v) BSA (Roth) depending on the antibody requirements for 1 hour. Immunostaining was performed in the corresponding buffer supplemented with the respective primary and secondary antibodies. Proteins were detected using Western Lightning enhanced chemiluminescence (ECL) Plus (Perkin Elmer) according to the instructions of the manufacturer. Chemiluminescence signal was detected using the Advance ECL Chemocam Imager (Intas Science Imaging). Band intensities were quantified using the LabImage 1D Software (v 4.1, Intas Science Imaging).

The following primary antibodies were used: rabbit polyclonal anti–phospho-PKR (T446) (Abcam; BSA; 1:500), rabbit polyclonal anti–rabbit-phospho-eIF2α (S51) (Cell Signaling Technology; BSA; 1:500), rabbit polyclonal anti-PKR (K-17) (Santa Cruz Biotechnology; milk; 1:1000) for GST-PKR titration experiment, rabbit polyclonal anti-PKR (Proteintech; BSA; 1:1000) for detection in other experiments, rabbit polyclonal anti-eIF2α (Cell Signaling Technology; BSA; 1:1000), rabbit polyclonal anti-GADD34 (Proteintech; milk; 1:1000), rabbit polyclonal anti–cyclin D1 (H-295) (Santa Cruz Biotechnology; BSA; 1:1000), mouse monoclonal anti–β-actin (Sigma-Aldrich; milk; 1:5000), mouse monoclonal anti-GAPDH (G-9) (Santa Cruz Biotechnology; milk; 1:10,000), and mouse monoclonal anti-GFP (Clontech; milk; 1:2000).

Protein half-lives

Huh7 cells (for eIF2α and PKR) or Huh7 GADD34 Puro cells (for GADD34) were treated with CHX (100 μg/ml; Sigma-Aldrich) and harvested at different times after treatment. Protein expression levels were measured by Western blotting and band intensities quantified using LabImage 1D as described above. Protein half-life was determined by normalization to loading control (β-actin) and compared to levels in untreated cells. Cyclin D served as control of short-lived protein.

Absolute quantification of eIF2α and PKR protein in cell lysates

Huh7 YFP-TIA1 Neo cells (2×10^6) with or without stable overexpression of PKR were seeded on 15-cm cell culture dishes. One day after seeding, cells were incubated with DMEM complete supplemented with IFN-α (100 IU/ml) or left untreated. Twenty-four hours after treatment, cells were detached by trypsinization, counted by fluorescence-activated cell sorting (FACS), and lysed in protein lysis buffer as described above. To ensure thorough lysis, lysates were subjected to three freeze/thaw cycles at −80°C before centrifugation. Total protein concentration was measured as described above. Lysates ($n = 8$) containing 20 μg of total protein were spiked with different amounts of recombinant GST-tagged eIF2α (Abnova, 5/10/15/22/33/50/75 ng), recombinant GST-tagged PKR kinase domain (Abcam, 1/2/3/4.4/6.7/10/12.5 ng), or protein lysis buffer. Samples were subjected to SDS-PAGE, Western blotting, and immunostaining as described above. Band intensities were quantified as described above, and recombinant protein titration intensities were used as standard curves to quantify average endogenous protein molecule numbers per cell.

Absolute quantification of GADD34 protein in cell lysates

Huh7 cells were reverse-transduced with lentivirus of pWPI GADD34-eGFP Puro for 30 hours, as previously described. To determine GADD34-eGFP molecule number per cell, a lysate of 1.75×10^5 cells (ca. 100 μg of total protein as determined by protein assay) was analyzed in triplicate by Western blotting. A dilution series (0.5/1/2.5/5/10 ng) of recombinant eGFP protein was used to generate a standard curve. Whole-lane signal of membranes probed with eGFP-specific antibody was used to determine the total molecule number of GADD34-eGFP expressed in the standard lysate, including degradation products. The average molecule number per cell was used to calculate levels of GADD34 in various experiments by analyzing the calibrated lysate on the same Western blot membranes. To this end, band intensities of full-length GADD34 and GADD34-eGFP were compared. GAPDH signal intensity was used as a loading control.

Single-cell transcript quantification using RNA FISH

To analyze cell-to-cell variability of transcript levels, we performed single-cell transcript quantification using the ViewRNA ISH Cell Assay Kit (Affymetrix). Huh7 cells (1.5×10^5) were seeded on coverslips in a six-well plate and infected with HCV (MOI = 10 $TCID_{50}$ per cell) or left uninfected. Twenty-four hours after infection, cells were treated with IFN-α (100 IU/ml; PBL) or left untreated. Forty-eight hours after infection, cells were fixed for 15 min in 4% paraformaldehyde in PBS. RNA FISH was performed as follows: (i) cell permeabilization with 100% ethanol for 45 min at 4°C, (ii) three 10-min wash steps with PBS, (iii) protein digest with the Protease QS diluted 1:12,000 in PBS for 5 min at room temperature, (iv) three 10-min wash steps with PBS, (v) first labeling for 30 min at 40°C with the fluorescent probes diluted 1:25 with prewarmed Probe Set Diluent QF, (vi) three 10-min wash steps with wash buffer, (vii) second labeling for 30 min at 40°C with the label probe mix (diluted 1:25 with prewarmed Probe Set Diluent QF), (viii) three 10-min wash steps with PBS, (ix) one 10-min wash step with double-distilled water, and (x) mounting coverlips on glass slides with ProLong Gold Antifade Mountant (Molecular Probes).

All fluorescently labeled probes were purchased from Affymetrix: *EIF2S1* (eIF2α) type 1 (#VA1-20426, diluted 1:50); *PPP1R15A* (GADD34) type 1 (#VA1-15768, diluted 1:50); *PRKR* (PKR) type 4 (#VA4-18296, diluted 1:50); and HCV (+)ssRNA type 6 (#VF6-13516, diluted 1:100). Probes targeting dapB transcripts were used as negative control (type 1 #VF1-11712 and type 4 #VF-4-10408, diluted 1:50). 5′ fluorescently labeled Oligo(dT)50 probes (Alexa Fluor 488 or Alexa Fluor 555) targeting mRNA poly(A) sequences were used at a final concentration of 50 nM to visualize cell outlines and SGs.

Images of whole cell volume (200 nm Z spacing) were acquired on a Nikon Ti Eclipse microscope equipped with a PerkinElmer UltraView Vox spinning disc CSU-X1, using the CFI Apo TIRF 60× (NA 1.49) oil objective (Nikon). Images were corrected for uneven illumination by division with an illumination bias mask and multiplying each pixel intensity by a factor of 2000 using the Fiji package software (http://fiji.sc) (*69*). Individual masks were generated for each channel by acquiring an image of autofluorescent plastic slides (Chromas) and processed by applying the Gaussian blur function in Fiji (radius 50).

To determine transcript levels on a single-cell level, a MATLAB-based software was developed to manually circle cells of interest and to assign individual phenotypes (infected/noninfected and stressed/nonstressed). For each dataset (two biological repeats) and fluorescent channel, negative control samples (uninfected cells hybridized with probes targeting prokaryotic dapB transcripts and HCV genome) were used to identify fixed size threshold (ST) and intensity thresholds (IT): GADD34 + HCV FISH – GADD34 [IT 750/1500, ST 25/15] and HCV [IT 750/1500, ST 10/15]; PKR + HCV FISH – PKR [IT 220/400, ST 10/6] and HCV [IT 500/1800, ST

15/10]; GADD34 + HCV FISH in PKR_{OE} – GADD34 [IT 6000, ST 10] and HCV [IT 1500, ST 10]. Applying these values, total transcript levels were calculated on a single-cell, multilayered phenotype level. Signals exceeding the IT and ST (determined in cells hybridized by negative control probes) are circled in white.

Single-cell Western blot analysis

Huh7 cells (10^5; naïve, PKR_{KO} clone 2#3, or PKR_{OE}) were seeded in six-well plates. Twenty-four hours after seeding, cells were treated with IFN-α (100 IU/ml) or left untreated. Twenty-four hours after treatment, cells were detached using Accutase (Capricorn). Single-cell Western blotting was performed using the Standard scWestern Kit (Proteinsimple) as recommended by the manufacturer. In short, 2 ml of cell suspension (4×10^5 cells) was loaded on dry slides, allowed to settle for 30 min, and carefully washed with suspension buffer. For PKR protein detection, 500 µl of Huh7 PKR_{KO} cell suspension was loaded on a separate section of the microslide as a background control. Well occupation rate (maximum 30%) and duplicates (maximum 2% of occupied wells) were monitored manually by light microscopy. Microslides were transferred to the MILO single-cell Western system (Proteinsimple) and subjected to 10-s lysis, 90-s electrophoresis at 240 V, and 240-s UV capture. Subsequently, slides were washed three times for 15 min in wash buffer and stained in primary antibodies (dilution 1:10 in Antibody Diluent 2) for 2 hours, followed by three washes of 15 min. Fluorescent secondary antibodies (dilution 1:20 in Antibody Diluent 2) were incubated for 90 min, followed by three washes of 15 min. For complete salt removal, slides were washed in double-distilled water twice for at least 2 hours. Last, slides were transferred to 50-ml reaction tubes and subjected to dry centrifugation for 1 hour at 1000*g*. Images were acquired using the InnoScan 710 microarray scanner (Innopsys) and the acquisition software Mapix (Innopsys, version 8.1.1). Correction for staining intensity variation was performed using Fiji by division of each image by a blurred mask of itself and subsequent pixel intensity multiplication by 2000. The masks were generated by applying Gaussian blur function (radius 200). Each well was manually curated by filtering out damaged or soiled regions of the chip using Scout 2.1 software (Proteinsimple). To determine total signal intensity per lane, a script was developed to automatically detect centers of wells and to segment total lane areas on each chip. Background intensity was determined using empty wells for eIF2α quantification or PKR_{KO} cells for PKR quantification. The following primary and secondary antibodies were used: mouse monoclonal anti-GAPDH (G-9) (Santa Cruz Biotechnology), rabbit polyclonal anti-eIF2α (Cell Signaling Technology), rabbit monoclonal anti-PKR (Proteintech), goat anti–mouse-Alexa532 (Invitrogen), and goat anti–rabbit-Alexa635 (Invitrogen).

In vitro synthesis of ssRNA of positive and negative polarity, hybridization of dsRNA and purification

The sequence of the prokaryotic ampicillin resistance gene was used as template for the synthesis of dsRNA (100, 200, and 400 bp). Primers used included the T7 RNA polymerase promoter sequence: Plus_For (5′-TAATACGACTCACTATAGGGAGTATTCAACATTTCCGTGTCGCCCTTAT-3′); Plus_100bp_Rev (5′-CATCTTTTACTTTCACCAGCGTTTCTGGGT-3′); Plus_200bp_Rev (5′-ATCATTGGAAAACGTTCTTCGGGGCGAAAA-3′); Minus_100bp_For (5′-TAATACGACTCACTATAGGTCTTTTACTTTCACCAGCGTTTCTGGGTGA-3′); Minus_200bp_For (5′-TAATACGACTCACTATAGGCATTGGAAAACGTTCTTCGGGGCGAAAACT-3′), and Minus_Rev (5′-ATGAGTATTCAACATTTCCGTGTCGCCCTT-3′). Forty–base pair dsRNA, including the first 40 bp of ampicillin resistance gene was synthesized by Metabion (5′-AUGAGUAUUCAACAUUUCCGUGUCGCCCUUAUUCCCUUUU-3′). PCR products were purified using the Nucleospin Gel and PCR Clean-Up kit (Macherey-Nagel). ssRNA of positive and negative polarity was synthesized by in vitro transcription and purified as described above, using 3 µg of PCR product as template in a 100-µl reaction. For hybridization, equimolar amounts of respective positive and negative ssRNA were incubated at 85°C for 10 min in hybridization buffer (25 mM Hepes and 50 mM NaCl) and gradually cooled to room temperature within 1 hour. dsRNA was precipitated by adding 10% (v/v) 2 M sodium acetate (pH 4.5) and 75% (v/v) isopropanol and incubation on ice for 2 hours. Precipitated dsRNA was pelleted at 20,000*g* for 45 min. Pellets were washed with 70% (v/v) ethanol and resuspended in RNase-free water. RNA concentration was determined by measuring absorbance at 260 nm. RNA integrity and secondary structures were analyzed on denaturing agarose gels.

Induction of SGs by dsRNA and chemical stressors

Huh7 cells (1.5×10^5) or Huh7 YFP-TIA1 cells were seeded in six-well plates containing glass coverslips. After 24 hours, medium was replaced with fresh medium containing varying concentrations of sodium arsenite (Sigma-Aldrich), thapsigargin (Biotrend), or dimethyl sulfoxide (DMSO, Merck Millipore). Samples were analyzed by Western blot, Phos-tag gel, or by immunofluorescence analyses. To determine p-eIF2α expression levels and visualize SG formations, cells were treated for 45 min with arsenite or 1 hour with thapsigargin. To determine GADD34 expression levels, cells were treated for 8 hours with DMSO or thapsigargin. To measure the response to dsRNA, cells were transfected for 16 hours with varying amounts of dsRNA using Lipofectamine 2000 (Invitrogen) with an RNA: transfectant ratio of 1:2 according to the manufacturer's instructions.

Quantification of SGs by immunofluorescence analysis

To quantify percentage of SG-positive cells after drug treatment, Huh7 cells were fixed for 15 min with 4% paraformaldehyde in PBS, permeabilized by incubation in 0.5% Triton X-100 in PBS for 5 min, and incubated in blocking buffer [5% horse serum (C.c.pro) and 5% sucrose in PBS] for 30 min. SGs were visualized using polyclonal rabbit anti-eIF3B (Bethyl Laboratories, 1:1000), diluted in blocking buffer for 1 hour, washed three times with PBS for 5 min, and incubated with donkey anti-rabbit secondary antibody coupled to Alexa Fluor 488 (Invitrogen, 1:2000). Coverslips were washed in PBS three times for 5 min before mounting on glass slides using Fluoromount G Reagent (Southern Biotech). For Huh7 YFP-TIA1 cells, coverslips were directly mounted on glass slides after fixation. Images were acquired with a Nikon Ti Eclipse fluorescence microscope using a CFI Plan Apo Lambda 20× objective (NA 0.75) (Nikon). Fluorescent signal was captured using an EMCCD camera C9100 (Hamamatsu) and the NIS-Elements AR software package (Nikon, version 4.30). The percentage of SG-positive cells was determined manually using Fiji Cell Counter plug-in.

Phos-tag polyacrylamide gel analysis

Phos-tag gel analysis was performed to detect the mobility shift of p-eIF2α, as previously described (*63*). A 10% resolving polyacrylamide

gel was supplemented with 70 μM Phos-tag acrylamide (Fujifilm Wako Chemicals) and 140 μM Mn^{2+} as recommended by the manufacturer. Before blotting, gels were incubated in transfer buffer [25 mM tris-HCl (pH 8.3), 150 mM glycine, and 20% methanol] supplemented with 1 mM EDTA for 10 min, followed by a 10-min wash step in transfer buffer in the absence of EDTA. Both basal and phosphorylated forms of eIF2α were visualized using eIF2α-specific antibody. Signal and band intensity were quantified as described above. The percentage of p-eIF2α was determined by dividing the intensity of the slowly migrating band (p-eIF2α) with the sum of both band intensities (p-eIF2α + eIF2α).

Inhibition of thapsigargin-induced SG formation by GADD34 overexpression

For GADD34 lentivirus production, 5×10^6 HEK 293T cells were seeded into 10-cm cell culture dishes. One hour before transfection, medium was replenished. For transfection, 6.4 μg of pWPI GADD34 Puro or pWPI Puro (control), 6.4 μg of packaging plasmid (pCMVΔ8.91), and 2.16 μg of the vector expressing the vesicular stomatitis virus envelope glycoprotein (pMD2.G) were mixed with OptiMEM (Gibco) to a final volume of 400 μl. Polyethylenimine (PEI) (Sigma-Aldrich) was diluted to 112.5 μg/ml in OptiMEM to a final volume of 400 μl. Solutions of plasmid and PEI were mixed, vortexed rigorously, and incubated for 20 min at room temperature. Transfection mix was added dropwise onto producer cells. Medium was replenished after 6 hours. Lentivirus supernatant was harvested at 48 and 72 hours after transfection and filtered with a 0.45-μm pore size membrane. For transient overexpression of GADD34, Huh7 cells were detached by trypsinization, and 10^5 cells were resuspended in lentivirus supernatant diluted with DMEM complete to a final volume of 2 ml and seeded in six-well plates. Thirty hours after transduction, cells were treated with 2 μM thapsigargin for 1 hour and subsequently harvested for Western blot and immunofluorescence analyses. Lentiviruses encoding for the antibiotic resistance gene (pWPI Puro) were used as control.

Bacterial expression and purification of his-PKR and his-eIF2α

His-PKR was expressed from pET-His-PKR in *E. coli* BL21 (DE3)-RIL (provided by C. Müller, Heidelberg) cultured at 37°C in auto-induction medium [1% (w/v) tryptone, 0,5% (w/v) yeast extracts, 1 mM $MgSO_4$, 0.5% glycerol, 0.05% glucose, 0.2% lactose monohydrate, 25 mM $(NH_4)_2SO_4$, 50 mM KH_2PO_4, 50 mM Na_2HPO_4, chloramphenicol (34 μg/ml), and kanamycin (50 μg/ml)] until reaching an OD_{600} (optical density at 600 nm) of 2.0 and then transferred to 18°C for 20 hours. Bacteria were pelleted at 6000*g* at 4°C for 15 min and stored at −80°C. The bacteria were resuspended in 5 ml/g bacteria lysis buffer pH 8.0 [50 mM Na_2HPO_4, 300 mM NaCl, 20 mM imidazole, 1 mM phenylmethylsulfonyl fluoride (PMSF), and cOmplete EDTA-free protease inhibitor cocktail (Roche)] and lysed in three homogenization cycles using EmulsiFlex C3 (Avestin). The lysate was centrifuged at 15,000*g* for 1 hour at 4°C, and the supernatant was incubated with Ni-NTA agarose beads (1 ml of 50% slurry; Macherey & Nagel) for 18 hours at 4°C while tumbling. Beads were pelleted by centrifugation at 500*g* for 10 min at 4°C and washed twice with 10 ml wash buffer (50 mM Na_2HPO_4, 300 mM NaCl, and 20 mM imidazole). Protein was eluted with 10 ml of elution buffer (50 mM Na_2HPO_4, 300 mM NaCl, and 250 mM imidazole) in 1.5-ml fractions. Eluate was dialyzed for 16 hours in storage buffer [10 mM tris (pH 7.5), 50 mM KCl, 2 mM $MgCl_2$, 10% glycerol, and 7 mM β-mercaptoethanol] using dialysis tubes with a 12,000 to 14,000 molecular weight cutoff. His-PKR was concentrated to at least 10 mg/ml using Vivaspin centrifugal concentrator 30 K (Sartorius), snap-frozen in liquid nitrogen, and stored at −80°C.

His-eIF2α was expressed as described above with the following modifications: The protein pellet was resuspended in modified lysis buffer [20 mM tris, 500 mM NaCl, 2 mM β-mercaptoethanol, 20 mM imidazole, 1 mM PMSF, and cOmplete EDTA-free protease inhibitor cocktail (pH 8.0) (Roche)]. Beads were washed in modified wash buffer (20 mM tris, 500 mM NaCl, 2 mM β-mercaptoethanol, and 20 mM imidazole). Protein was eluted using modified elution buffer (20 mM tris, 500 mM NaCl, 2 mM β-mercaptoethanol, and 500 mM imidazole). Fractions containing the protein were identified by SDS-PAGE using Coomassie stain or Bio-Rad 12% TGX Stain-Free FastCast gels. The fractions containing His-eIF2α were pooled and dialyzed into ion exchange buffer A [20 mM bis-tris (pH 6.0) and 2 mM β-mercaptoethanol] for 16 hours at 4°C. Precipitate was separated by centrifugation at 15,000*g* for 5 min at 4°C followed by an anion exchange chromatography loading the supernatant on a HiTrap Q HP 5-ml column (GE Healthcare) and intensive wash step of 20 column volumes with ion exchange buffer A. Protein was eluted by a gradient of 0 to 100% ion exchange buffer B [20 mM bis-tris (pH 6.0), 500 mM NaCl, and 2 mM β-mercaptoethanol]. Clean fractions were pooled and concentrated to at least 10 mg/ml using Vivaspin centrifugal concentrator 10 K (Sartorius), snap-frozen in liquid nitrogen, and stored at −80°C. To remove hyperphosphorylation from His-PKR expressed in *E. coli*, the purified protein was subjected to dephosphorylation [adapted from (*70*)]. His-PKR (100 μg) was dephosphorylated using 3200 units of λ-PPase (New England Biolabs) in 200 μl of reaction buffer [50 mM Hepes, 100 mM NaCl, 2 mM DTT, 0.01% Brij 35 (pH 7.5), and 1 mM $MnCl_2$] for 2 hours at 37°C. The dephosphorylation reaction was stopped by the addition of 2 μl of 200 mM sodium orthovanadate and further incubation for 5 min at 37°C. Protein aggregates were removed by centrifugation for 30 min at 20,000*g* at 4°C. Protein concentration was determined by subjecting samples and dilution series of GST-PKR kinase domain (Abcam) to SDS-PAGE, followed by protein visualization by silver staining using the Silver Stain Plus Kit (Bio-Rad) following the manufacturer's instructions. Band intensity was quantified as described above.

In vitro PKR kinase assay

The protocol was adapted from (*70*). The reaction mix was prepared on ice in a final volume of 12 μl containing 150 ng of dephosphorylated His-PKR and 1 μg of His-eIF2α in activation buffer [20 mM Hepes (pH 7.5), 4 mM $MgCl_2$, and 100 mM KCl] supplemented with 1 mM Ultra-Pure ATP (Promega). Three microliters of dsRNA dilutions or water was added to the mix, and reactions were immediately incubated at 30°C for 20 min. Phosphatase activity was inhibited by the addition of 2 μl of 20 mM sodium orthovanadate. A total of 3.5 μl of 6× Laemmli buffer was added to the reaction mix, and samples were boiled at 95°C for 5 min. Half of the reaction (75 ng of PKR and 500 ng of eIF2α) was analyzed by SDS-PAGE, and total protein was visualized by Silver stain (see below); 1.67% of the reaction (2.5 ng of PKR and 16.7 ng of eIF2α) was analyzed by either SDS-PAGE or Phos-tag polyacrylamide gel as described above.

qRT-PCR of GADD34 mRNA and pre-mRNA

Huh7 cells (8×10^4) were seeded in a 12-well plate and treated with 2 μM thapsigargin for up to 12 hours. Cells were harvested 0, 1, 3, 6, and 12 hours after treatment, and total RNA was extracted as described above. Levels of mature GADD34 mRNA were determined using the qPCRBIO Probe 1-Step Go Lo-ROX, PCR Biosystems kit (Nippon Genetics). In brief, 15 μl of reaction mixes contained 7.5 μl of 2 × qPCRBIO mix, 0.75 μl of 20 × RTase, 400 nM per primer, 200 nM per probe, and 3 μl of extracted total RNA. For absolute quantification, serial 1:10 dilution series (10^3 to 10^9 copies) of GADD34 and GAPDH transcripts were processed on each plate. Each sample was measured in triplicate wells. Quantitative reverse transcription PCR (qRT-PCR) was performed on a CFX96 Real-Time System (Bio-Rad) using the following settings: 50°C for 10 min, 95°C for 1 min, and 40 cycles as follows: 95°C for 10 s and 60°C for 1 min. The following primers and probes were used to detect cellular transcripts: GAPDH_For: 5′-GAAGGTGAAGGTCGGAGTC-3′; GAPDH_Rev: 5′-GAAGATGGTGATGGGATTTC-3′; GAPDH_Probe: 5′-VIC–CAAGCTTCCCGTTCTCAGCCT–TAMRA-3′; GADD34mRNA_For: 5′-CAGAAACCCCTACTCATGATCC-3′, GADD34mRNA_Rev: 5′-AAATGGACAGTGACCTTCTCG-3′, GADD34_Probe: 5′-FAM–CCCCTAAAGGCCAGAAAGGTGCGC–TAMRA-3′. GAPDH copy number was used for normalization. For the detection of GADD34 pre-mRNA, 30 μl of total RNA was incubated with 1 μl of TURBO DNase and TURBO DNase buffer (Invitrogen) in a total volume of 50 μl at 37°C for 30 min to remove genomic DNA. Next, 3 μl of DNase-digested RNA was reverse-transcribed into cDNA using the Applied Biosystems High Capacity cDNA Reverse Transcription kit (Thermo Fisher Scientific) as recommended by the manufacturer (25°C for 10 min, 37°C for 2 hours, and 85°C for 5 min). The cDNA was diluted 1:20 before detection of GADD34 pre-mRNA transcripts using iTaq Universal SYBR Green (Bio-Rad). In short, 15 μl of mix contained 7.5 μl of 2× iTaq mix, 500 nM per primer, and 3 μl of prediluted cDNA. Each sample was measured in triplicate wells. qRT-PCR was performed on a CFX96 Real-Time System (Bio-Rad) using the following settings: 95°C for 3 min and 45 cycles as follows: 95°C for 10 s and 60°C for 30 s. The following primers were used: GADD34prem:For: 5′-ACAGTGACAGGCAAGTGACTAG-3′ and GADD34prem:Rev: 5′-GGAAGAGAGAGAGAGAAGCAAAC-3′;GAPDH_For:5′-GAAGGTGAAGGTCGGAGTC-3′ and GAPDH_Rev: 5′-GAAGATGGTGATGGGATTTC-3′. GAPDH mRNA was used for normalization. RT-PCR data were analyzed by using the ΔΔCT method (*71*).

Statistical analysis

Statistical analysis was performed by using the GraphPad Prism software (version 7.04). Statistical significance for Western blot, Phos-tag gel, and SG immunofluorescence analyses was calculated by performing two-way ANOVA with Dunnett's multiple comparisons test. Statistical significance for FISH analyses was calculated by performing two-tailed unpaired *t* test with Welch's correction. $^*P < 0.05$; $^{**}P < 0.01$; $^{***}P < 0.001$; $^{****}P < 0.0001$.

SUPPLEMENTARY MATERIALS

Supplementary material for this article is available at https://science.org/doi/10.1126/sciadv.abk2022

View/request a protocol for this paper from *Bio-protocol*.

REFERENCES AND NOTES

1. K. Pakos-Zebrucka, I. Koryga, K. Mnich, M. Ljujic, A. Samali, A. M. Gorman, The integrated stress response. *EMBO Rep.* **17**, 1374–1395 (2016).
2. M. Holcik, N. Sonenberg, Translational control in stress and apoptosis. *Nat. Rev. Mol. Cell Biol.* **6**, 318–327 (2005).
3. S. Hofmann, N. Kedersha, P. Anderson, P. Ivanov, Molecular mechanisms of stress granule assembly and disassembly. *Biochim Biophys Acta Mol Cell Res* **1868**, 118876 (2021).
4. E. Meurs, K. Chong, J. Galabru, N. S. B. Thomas, I. M. Kerr, B. R. G. Williams, A. G. Hovanessian, Molecular cloning and characterization of the human double-stranded RNA-activated protein kinase induced by interferon. *Cell* **62**, 379–390 (1990).
5. N. Eiermann, K. Haneke, Z. Sun, G. Stoecklin, A. Ruggieri, Dance with the devil: Stress granules and signaling in antiviral responses. *Viruses* **12**, (2020).
6. A. C. Dar, T. E. Dever, F. Sicheri, Higher-order substrate recognition of eIF2alpha by the RNA-dependent protein kinase PKR. *Cell* **122**, 887–900 (2005).
7. M. Dey, C. Cao, A. C. Dar, T. Tamura, K. Ozato, F. Sicheri, T. E. Dever, Mechanistic link between PKR dimerization, autophosphorylation, and eIF2alpha substrate recognition. *Cell* **122**, 901–913 (2005).
8. P. A. Lemaire, E. Anderson, J. Lary, J. L. Cole, Mechanism of PKR activation by dsRNA. *J. Mol. Biol.* **381**, 351–360 (2008).
9. R. C. Patel, P. Stanton, N. M. McMillan, B. R. Williams, G. C. Sen, The interferon-inducible double-stranded RNA-activated protein kinase self-associates in vitro and in vivo. *Proc. Natl. Acad. Sci. U.S.A.* **92**, 8283–8287 (1995).
10. E. Kojima, A. Takeuchi, M. Haneda, A. Yagi, T. Hasegawa, K. Yamaki, K. Takeda, S. Akira, K. Shimokata, K. Isobe, The function of GADD34 is a recovery from a shutoff of protein synthesis induced by ER stress: Elucidation by GADD34-deficient mice. *FASEB J.* **17**, 1573–1575 (2003).
11. A. Ruggieri, E. Dazert, P. Metz, S. Hofmann, J. P. Bergeest, J. Mazur, P. Bankhead, M. S. Hiet, S. Kallis, G. Alvisi, C. E. Samuel, V. Lohmann, L. Kaderali, K. Rohr, M. Frese, G. Stoecklin, R. Bartenschlager, Dynamic oscillation of translation and stress granule formation mark the cellular response to virus infection. *Cell Host Microbe* **12**, 71–85 (2012).
12. B. Novak, J. J. Tyson, Design principles of biochemical oscillators. *Nat. Rev. Mol. Cell Biol.* **9**, 981–991 (2008).
13. Y. Cao, A. Lopatkin, L. You, Elements of biological oscillations in time and space. *Nat. Struct. Mol. Biol.* **23**, 1030–1034 (2016).
14. Z. Li, Q. Yang, Systems and synthetic biology approaches in understanding biological oscillators. *Quant. Biol.* **6**, 1–14 (2018).
15. M. B. Elowitz, A. J. Levine, E. D. Siggia, P. S. Swain, Stochastic gene expression in a single cell. *Science* **297**, 1183–1186 (2002).
16. A. Raj, C. S. Peskin, D. Tranchina, D. Y. Vargas, S. Tyagi, Stochastic mRNA synthesis in mammalian cells. *PLoS Biol.* **4**, e309 (2006).
17. A. Raj, A. van Oudenaarden, Nature, nurture, or chance: Stochastic gene expression and its consequences. *Cell* **135**, 216–226 (2008).
18. E. M. Ozbudak, M. Thattai, I. Kurtser, A. D. Grossman, A. van Oudenaarden, Regulation of noise in the expression of a single gene. *Nat. Genet.* **31**, 69–73 (2002).
19. S. Skylaki, O. Hilsenbeck, T. Schroeder, Challenges in long-term imaging and quantification of single-cell dynamics. *Nat. Biotechnol.* **34**, 1137–1144 (2016).
20. S. Berg, D. Kutra, T. Kroeger, C. N. Straehle, B. X. Kausler, C. Haubold, M. Schiegg, J. Ales, T. Beier, M. Rudy, K. Eren, J. I. Cervantes, B. Xu, F. Beuttenmueller, A. Wolny, C. Zhang, U. Koethe, F. A. Hamprecht, A. Kreshuk, ilastik: Interactive machine learning for (bio) image analysis. *Nat Methods* **16**, 1226–1232 (2019).
21. S. Taniuchi, M. Miyake, K. Tsugawa, M. Oyadomari, S. Oyadomari, Integrated stress response of vertebrates is regulated by four eIF2α kinases. *Sci. Rep.* **6**, 32886 (2016).
22. K. Sneppen, S. Krishna, S. Semsey, Simplified models of biological networks. *Annu. Rev. Biophys.* **39**, 43–59 (2010).
23. M. H. Brush, S. Shenolikar, Control of cellular GADD34 levels by the 26S proteasome. *Mol. Cell. Biol.* **28**, 6989–7000 (2008).
24. T. Hunter, T. Hunt, R. J. Jackson, H. D. Robertson, The characteristics of inhibition of protein synthesis by double-stranded ribonucleic acid in reticulocyte lysates. *J. Biol. Chem.* **250**, 409–417 (1975).
25. M. Dey, B. R. Mann, A. Anshu, M. A. Mannan, Activation of protein kinase PKR requires dimerization-induced cis-phosphorylation within the activation loop. *J. Biol. Chem.* **289**, 5747–5757 (2014).
26. C. B. Mayo, H. Erlandsen, D. J. Mouser, A. G. Feinstein, V. L. Robinson, E. R. May, J. L. Cole, Structural basis of protein kinase R autophosphorylation. *Biochemistry* **58**, 2967–2977 (2019).
27. I. Novoa, H. Zeng, H. P. Harding, D. Ron, Feedback inhibition of the unfolded protein response by GADD34-mediated dephosphorylation of eIF2alpha. *J. Cell Biol.* **153**, 1011–1022 (2001).
28. H. P. Harding, I. Novoa, Y. Zhang, H. Zeng, R. Wek, M. Schapira, D. Ron, Regulated translation initiation controls stress-induced gene expression in mammalian cells. *Mol. Cell* **6**, 1099–1108 (2000).
29. T. W. Fawcett, J. L. Martindale, K. Z. Guyton, T. Hai, N. J. Holbrook, Complexes containing activating transcription factor (ATF)/cAMP-responsive-element-binding protein (CREB) interact with the CCAAT/enhancer-binding protein (C/EBP)-ATF composite site to regulate Gadd153 expression during the stress response. *Biochem. J.* **339** (Pt. 1), 135–141 (1999).

30. H. M. Lazear, A. Lancaster, C. Wilkins, M. S. Suthar, A. Huang, S. C. Vick, L. Clepper, L. Thackray, M. M. Brassil, H. W. Virgin, J. Nikolich-Zugich, A. V. Moses, M. Gale, K. Früh, M. S. Diamond, IRF-3, IRF-5, and IRF-7 coordinately regulate the type I IFN response in myeloid dendritic cells downstream of MAVS signaling. *PLOS Pathog.* **9**, e1003118 (2013).
31. A. Dalet, R. J. Argüello, A. Combes, L. Spinelli, S. Jaeger, M. Fallet, T. P. Vu Manh, A. Mendes, J. Perego, M. Reverendo, V. Camosseto, M. Dalod, T. Weil, M. A. Santos, E. Gatti, P. Pierre, Protein synthesis inhibition and GADD34 control IFN-β heterogeneous expression in response to dsRNA. *EMBO J.* **36**, 761–782 (2017).
32. S. Legewie, H. Herzel, H. V. Westerhoff, N. Bluthgen, Recurrent design patterns in the feedback regulation of the mammalian signalling network. *Mol. Syst. Biol.* **4**, 190 (2008).
33. A. Borsch, J. Schaber, How time delay and network design shape response patterns in biochemical negative feedback systems. *BMC Syst. Biol.* **10**, 82 (2016).
34. Y. Y. Lee, R. C. Cevallos, E. Jan, An upstream open reading frame regulates translation of GADD34 during cellular stresses that induce eIF2alpha phosphorylation. *J. Biol. Chem.* **284**, 6661–6673 (2009).
35. W. Ma, A. Trusina, H. El-Samad, W. A. Lim, C. Tang, Defining network topologies that can achieve biochemical adaptation. *Cell* **138**, 760–773 (2009).
36. C. Jia, M. Qian, Nonequilibrium enhances adaptation efficiency of stochastic biochemical systems. *PLOS ONE* **11**, e0155838 (2016).
37. M. Ebisuya, K. Kondoh, E. Nishida, The duration, magnitude and compartmentalization of ERK MAP kinase activity: Mechanisms for providing signaling specificity. *J. Cell Sci.* **118**, 2997–3002 (2005).
38. D. T. Gillespie, Exact stochastic simulation of coupled chemical reactions. *J. Phys. Chem.* **81**, 2340–2361 (1977).
39. B. Schwanhausser, D. Busse, N. Li, G. Dittmar, J. Schuchhardt, J. Wolf, W. Chen, M. Selbach, Global quantification of mammalian gene expression control. *Nature* **473**, 337–342 (2011).
40. E. L. Ellis, M. Delbruck, The growth of bacteriophage. *J. Gen. Physiol.* **22**, 365–384 (1939).
41. A. J. Hughes, D. P. Spelke, Z. Xu, C. C. Kang, D. V. Schaffer, A. E. Herr, Single-cell Western blotting. *Nat. Methods* **11**, 749–755 (2014).
42. A. Trusina, F. R. Papa, C. Tang, Rationalizing translation attenuation in the network architecture of the unfolded protein response. *Proc. Natl. Acad. Sci. U.S.A.* **105**, 20280–20285 (2008).
43. A. Trusina, C. Tang, The unfolded protein response and translation attenuation: A modelling approach. *Diabetes Obes. Metab.* **12** (Suppl. 2), 27–31 (2010).
44. D. R. Diedrichs, J. A. Gomez, C. S. Huang, D. T. Rutkowski, R. Curtu, A data-entrained computational model for testing the regulatory logic of the vertebrate unfolded protein response. *Mol. Biol. Cell* **29**, 1502–1517 (2018).
45. D. T. Rutkowski, S. M. Arnold, C. N. Miller, J. Wu, J. Li, K. M. Gunnison, K. Mori, A. A. Sadighi Akha, D. Raden, R. J. Kaufman, Adaptation to ER stress is mediated by differential stabilities of pro-survival and pro-apoptotic mRNAs and proteins. *PLoS Biol.* **4**, e374 (2006).
46. H. Yang, M. Niemeijer, B. van de Water, J. B. Beltman, ATF6 is a critical determinant of CHOP Dynamics during the unfolded protein response. *iScience* **23**, 100860 (2020).
47. K. Erguler, M. Pieri, C. Deltas, A mathematical model of the unfolded protein stress response reveals the decision mechanism for recovery, adaptation and apoptosis. *BMC Syst. Biol.* **7**, 16 (2013).
48. N. E. Phillips, C. Manning, N. Papalopulu, M. Rattray, Identifying stochastic oscillations in single-cell live imaging time series using Gaussian processes. *PLoS Comput. Biol.* **13**, e1005479 (2017).
49. J. R. Wheeler, T. Matheny, S. Jain, R. Abrisch, R. Parker, Distinct stages in stress granule assembly and disassembly. *eLife* **5**, e18413 (2016).
50. H. H. Rabouw, M. A. Langereis, A. A. Anand, L. J. Visser, R. J. de Groot, P. Walter, F. J. M. van Kuppeveld, Small molecule ISRIB suppresses the integrated stress response within a defined window of activation. *Proc. Natl. Acad. Sci. U.S.A.* **116**, 2097–2102 (2019).
51. M. Brocard, V. Iadevaia, P. Klein, B. Hall, G. Lewis, J. Lu, J. Burke, M. M. Willcocks, R. Parker, I. G. Goodfellow, A. Ruggieri, N. Locker, Norovirus infection results in eIF2α independent host translation shut-off and remodels the G3BP1 interactome evading stress granule formation. *PLOS Pathog.* **16**, e1008250 (2020).
52. A. Leroux, I. M. London, Regulation of protein synthesis by phosphorylation of eukaryotic initiation factor 2 alpha in intact reticulocytes and reticulocyte lysates. *Proc. Natl. Acad. Sci. U.S.A.* **79**, 2147–2151 (1982).
53. B. Husain, I. Mukerji, J. L. Cole, Analysis of high-affinity binding of protein kinase R to double-stranded RNA. *Biochemistry* **51**, 8764–8770 (2012).
54. P. A. Lemaire, J. Lary, J. L. Cole, Mechanism of PKR activation: Dimerization and kinase activation in the absence of double-stranded RNA. *J. Mol. Biol.* **345**, 81–90 (2005).
55. S. A. McKenna, D. A. Lindhout, I. Kim, C. W. Liu, V. M. Gelev, G. Wagner, J. D. Puglisi, Molecular framework for the activation of RNA-dependent protein kinase. *J. Biol. Chem.* **282**, 11474–11486 (2007).
56. L. G. Ortega, M. McCotter, G. L. Henry, S. McCormack, D. C. Thomis, C. E. Samuel, Mechanism of interferon action. Biochemical and genetic evidence for the intermolecular association of the RNA-dependent protein kinase PKR from human cells. *Virology* **215**, 31–39 (1996).
57. I. Romero-Brey, R. Bartenschlager, Endoplasmic reticulum: The favorite intracellular niche for viral replication and assembly. *Viruses* **8**, 160 (2016).
58. J. T. Mettetal, D. Muzzey, C. Gomez-Uribe, A. van Oudenaarden, The frequency dependence of osmo-adaptation in *Saccharomyces cerevisiae*. *Science* **319**, 482–484 (2008).
59. H. El-Samad, J. P. Goff, M. Khammash, Calcium homeostasis and parturient hypocalcemia: An integral feedback perspective. *J. Theor. Biol.* **214**, 17–29 (2002).
60. N. Barkai, S. Leibler, Robustness in simple biochemical networks. *Nature* **387**, 913–917 (1997).
61. K. F. Sonnen, A. Aulehla, Dynamic signal encoding—From cells to organisms. *Semin. Cell Dev. Biol.* **34**, 91–98 (2014).
62. M. M. Fay, D. Columbo, C. Cotter, C. Friend, S. Henry, M. Hoppe, P. Karabelas, C. Lamy, M. Lawell, S. Monteith, C. Noyes, P. Salerno, J. Wu, H. M. Zhang, P. J. Anderson, N. Kedersha, P. Ivanov, N. G. Farny, Bisphenol A promotes stress granule assembly and modulates the integrated stress response. *Biol. Open* **10**, bio067539 (2021).
63. H. Roth, V. Magg, F. Uch, P. Mutz, P. Klein, K. Haneke, V. Lohmann, R. Bartenschlager, O. T. Fackler, N. Locker, G. Stoecklin, A. Ruggieri, Flavivirus infection uncouples translation suppression from cellular stress responses. *mBio* **8**, 02150-16 (2017).
64. K. J. Blight, J. A. McKeating, C. M. Rice, Highly permissive cell lines for subgenomic and genomic hepatitis C virus RNA replication. *J. Virol.* **76**, 13001–13014 (2002).
65. E. Steinmann, C. Brohm, S. Kallis, R. Bartenschlager, T. Pietschmann, Efficient trans-encapsidation of hepatitis C virus RNAs into infectious virus-like particles. *J. Virol.* **82**, 7034–7046 (2008).
66. S. Reiss, I. Rebhan, P. Backes, I. Romero-Brey, H. Erfle, P. Matula, L. Kaderali, M. Poenisch, H. Blankenburg, M. S. Hiet, T. Longerich, S. Diehl, F. Ramirez, T. Balla, K. Rohr, A. Kaul, S. Bühler, R. Pepperkok, T. Lengauer, M. Albrecht, R. Eils, P. Schirmacher, V. Lohmann, R. Bartenschlager, Recruitment and activation of a lipid kinase by hepatitis C virus NS5A is essential for integrity of the membranous replication compartment. *Cell Host Microbe* **9**, 32–45 (2011).
67. T. Pietschmann, A. Kaul, G. Koutsoudakis, A. Shavinskaya, S. Kallis, E. Steinmann, K. Abid, F. Negro, M. Dreux, F. L. Cosset, R. Bartenschlager, Construction and characterization of infectious intragenotypic and intergenotypic hepatitis C virus chimeras. *Proc. Natl. Acad. Sci. U.S.A.* **103**, 7408–7413 (2006).
68. B. D. Lindenbach, M. J. Evans, A. J. Syder, B. Wölk, T. L. Tellinghuisen, C. C. Liu, T. Maruyama, R. O. Hynes, D. R. Burton, J. A. McKeating, C. M. Rice, Complete replication of hepatitis C virus in cell culture. *Science* **309**, 623–626 (2005).
69. J. Schindelin, I. Arganda-Carreras, E. Frise, V. Kaynig, M. Longair, T. Pietzsch, S. Preibisch, C. Rueden, S. Saalfeld, B. Schmid, J. Y. Tinevez, D. J. White, V. Hartenstein, K. Eliceiri, P. Tomancak, A. Cardona, Fiji: An open-source platform for biological-image analysis. *Nat. Methods* **9**, 676–682 (2012).
70. T. Matsui, K. Tanihara, T. Date, Expression of unphosphorylated form of human double-stranded RNA-activated protein kinase in *Escherichia coli*. *Biochem. Biophys. Res. Commun.* **284**, 798–807 (2001).
71. K. J. Livak, T. D. Schmittgen, Analysis of relative gene expression data using real-time quantitative PCR and the 2−ΔΔCT method. *Methods* **25**, 402–408 (2001).
72. D. J. Odde, H. M. Buettner, Autocorrelation function and power spectrum of two-state random processes used in neurite guidance. *Biophys. J.* **75**, 1189–1196 (1998).
73. T. Maiwald, J. Timmer, Dynamical modeling and multi-experiment fitting with PottersWheel. *Bioinformatics* **24**, 2037–2043 (2008).
74. N. Zeng, Y. Li, L. He, X. Xu, V. Galicia, C. Deng, B. L. Stiles, Adaptive basal phosphorylation of eIF2α is responsible for resistance to cellular stress-induced cell death in Pten-Null hepatocytes. *Mol. Cancer Res.* **9**, 1708–1717 (2011).
75. J. Feigelman, S. Ganscha, M. Claassen, matLeap: A fast adaptive Matlab-ready tau-leaping implementation suitable for Bayesian inference. *arXiv* 1608.07058 (2016).

Acknowledgments: We thank M. Langlotz from the ZMBH Flow Cytometry and FACS Core Facility (Heidelberg University) for support in cell sorting, V. Laketa from the Infectious Diseases Imaging Platform (IDIP) at the CIID (Heidelberg University), D. Scholz and K. Nettesheim from Nikon Instruments Germany for assistance and support with live-cell microscopy, G. Stier and I. Sinning (BZH, Heidelberg University) for providing the pET His 1a vector, and H. Herzel, M. Binder, and J. Timmer for critical discussions. **Funding:** This study was supported by Deutsche Forschungsgemeinschaft (DFG, German Research Foundation) - project number 240245660 (TP13 to A.R., TP8 to O.T.F., TP11 to R.B. and T.H., and Z4 to F.A.H. and K. Roh), DFG - project number 278001972 (A14 to A.R. and G.S. and A21N to T.H.), DFG - project number 272983813 (TP12 to A.R. and TP9 to R.B.), equipment program of Cellnetworks Cluster of Excellence (EXOC 81) (funds for MILO single-cell Western system to

O.T.F.), and Bundesministerium Bildung und Forschung (BMBF) - project number 031L0270 to S.M.K. (Computational Life Sciences program). **Author contributions:** A.R. conceived the study, and designed and interpreted the experiments. P.K. additionally designed, performed, and analyzed the experiments. S.M.K. designed and performed all computational analyses and mathematical modeling and supported image analysis. A.R., P.K., and S.M.K. wrote the manuscript with input from all authors. H.R. and V.M. performed experiments. T.B.N.L.-H. generated recombinant His-tagged PKR and eIF2α proteins. P.K., K. Rot., J.A., Y.Q., and S.W. performed the image analysis under the guidance of F.A.H. and K. Roh. O.O. provided technical expertise with FISH analysis. R.K. and B.D.V. developed a preliminary version of the deterministic model. R.E., R.B., and O.T.F. provided guidance and infrastructure. S.R.T., O.T.F., T.H., and G.S. reviewed and edited the manuscript. **Competing interests:** The authors declare that they have no competing interests. **Data and materials availability:** All data needed to evaluate the conclusions in the paper are present in the paper and/or the Supplementary Materials. Cell lines and plasmids are available by material transfer agreement. Requests are to be sent to A.R. (alessia.ruggieri@med.uni-heidelberg.de).

Submitted 28 June 2021
Accepted 20 January 2022
Published 23 March 2022
10.1126/sciadv.abk2022